National Taras Shevchenko University of Kiev
Faculty for Physics
Nuclear Physics Department

High-transverse energy photons with accompanying jet in deep inelastic scattering in ZEUS

Specialty: 8.070103 – physics
Specialization: experimental nuclear physics

Master thesis
from 5th year student
Volynets Oleksandr

Supervisors:
Dr. Prof. I.N.Kadenko (Kiev, Ukraine)
Dr. Prof. P.Bussey (Glasgow, UK)

Kiev-Hamburg 2009

Contents

1 Introduction

For many centuries people have been trying to understand the structure of everything on Earth. Last century physicists made a large step forward to matter structure understanding. After the discovery that everything consists of atoms, it was later found out that atoms consist of electrons, protons and neutrons. Later on people managed to describe the things that could not be imagined. The quantum mechanics appeared as a new science, which gave a stimulus for further Universe processes understanding. Advancing ideas of quantum mechanics, ones managed to look even closer to the structure of protons, neutrons and other particles, which led to developing the quantum chromodynamics.

Present work is based on the ZEUS data, which is located in one of 4 experimental halls of HERA electron-proton collider in DESY research center (Hamburg, Germany). The main tasks of this experiment were studying of proton structure function, quantum chromodynamics etc.

The prompt photon analysis is one of the most important parts of the deep inelastic scattering physics. Photons with high transverse energy produced during high-energy collisions are a powerful tool for researches in the parton dynamics and hadron structure. Such photons (called "prompt photons", or "direct photons") are one of first products during electron-proton interaction. Also during many analyses the effect of hadronization should be taken into account. It is not yet completely understood. This effect can be omitted in the present analysis since there is no hadronization of prompt photons and it is easier to deal with them.

The main goal of the present analysis was to measure differential cross section of prompt photons as a function of photon variables, transverse energy and pseudorapidity, and event variables, exchange photon virtuality and Bjorken scale variable for the reaction $ep \to e\gamma X$ with center-of-mass energy of 318 GeV in deep inelastic scattering with high virtuality of exchanged photon.

Prompt photon plus jet analysis which is also discussed in the present thesis give the opportunity to compare with the theoretical QCD NLO calculation with better precision as for the inclusive prompt photon analysis.

Chapter 2 gives a introduction to theory of lepton-nucleon scattering and prompt photons production. Chapter 4 and 5 provides a short description of

the ZEUS experiment with it's main parts and HERA accelerator. Chapter 6 and 8 describes the event selection and signal extraction for the prompt photons. Chapter 7 gives an explanation of the jet finding algorithms and the event selection for the jets. Chapters 9.3 and 10.4 present results of measuring differential cross section for the inclusive analysis and prompt photon plus jet analysis respectively.

2 Theory

HERA accelerator [1] is a unique electron-proton accelerator with record short wavelength of electron, and that is why this superelectron microscope provides unique possibility to study the inner structure of proton. It is a perfect tool to verify QCD predictions. In particular this type of interactions gives a possibility to measure numerically the quark-gluon proton structure and measure cross section of many processes and compare results with theory.

2.1 Lepton-nucleon scattering

In the most general situation interactions between electron and proton occur with the virtual boson exchange. In case the energy of the exchanged boson is not enough to destroy the proton, and so the particles interact via elastic scattering (see fig. 2.1).

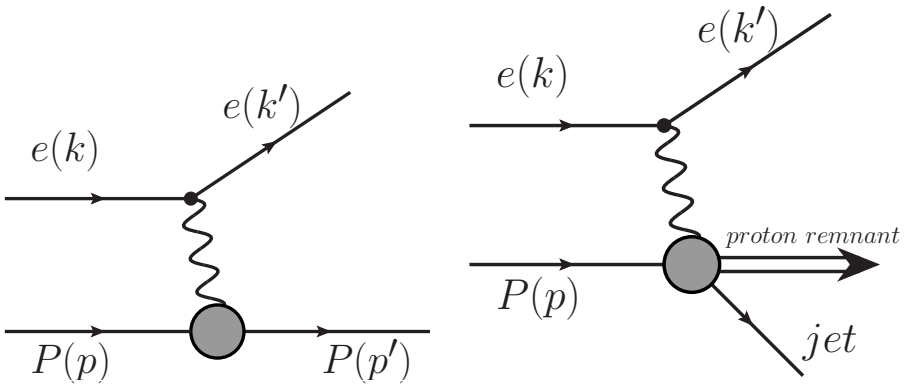

Figure 2.1: Elastic (a) and deep inelastic (b) scattering in *ep* collisions

Exchanged boson has 4-momenta $q = k' - k$, where k' and k are defined as the 4-momentums of scattered and initial electron respectively. The parameter of inelasticity of the process is defined as $Q^2 = -q^2 = (k' - k)^2$. In case the exchanged boson is a photon this parameter is also called a photon virtuality.

As Q^2 increase the exchanged boson becomes more and more virtual. Thus it gets the ability to resolve the internal quark structure of the proton, and the consideration of quark-boson interaction is necessary. The proton does not interact as a single unit anymore. The resolved quark scatters off the boson and the proton remnant continues largely undeviated from its original direction. The possible value of Q^2 that could be reached at HERA were between 0 and 40000 GeV^2.

Hence there are two types of scattering which can occur - elastic and inelastic. The total cross section of ep interactions are inversely proportional to Q^4: $\sigma \sim \frac{1}{Q^4}$, so the elastic scattering occurs mostly at low Q^2. No quarks are resolved from the proton. The other type of scattering is known as Deep Inelastic Scattering, DIS (see Fig. 2.1), and occurs at high Q^2 [1] where one quark (or gluon) is resolved from the proton. The region of Q^2 close to 0 is known as photoproduction and extensive studies of prompt photon production have been performed in this region.

2.2 HERA kinematic parameters

Electron-proton scattering events are characteristically described in terms of their Q^2 and x values at a given center of mass energy $\sqrt{s}$, where Q^2 is as previously defined and x is the dimensionless Bjorken scaling variable. The two dimensionless variables x and y are defined by the relationship in Equations 2.1 and 2.2

$$x = \frac{-q^2}{2p \cdot q} \tag{2.1}$$

$$y = \frac{q \cdot p}{k \cdot p} \tag{2.2}$$

[1] The arbitrary value of $Q^2 > 1\text{GeV}^2$ can be considered, though usually in the experiment $Q^2 > 4..10$ GeV^2 are used as the Monte Carlo do not describe lower region well

where p is the 4-momentum of the proton. The quantity $q = (k - k')$ denotes the 4-momentum transfer from the electron. In the parton model, x can be interpreted as the proton momentum fraction carried by struck quark. The equation 2.3 gives the definition of the center of mass energy.

$$s = (k + p)^2 = 4E_e E_p \tag{2.3}$$

During deep inelastic scattering the electron deviate from its initial direction, and thus is easy detected by calorimeter. The main characteristics measured in experiment is $\sum_i E_i - p_{zi}$ where the sum of momentums and energy over all calorimeter cells.

The main parameters of particles produced during the interaction are as follows: $E_T = E \cdot sin\theta$ – transverse energy, and $\eta = -log\left(tg\left(\frac{\theta}{2}\right)\right)$ – pseudorapidity, where θ – polar angle of particle in ZEUS coordinate system (see. Chapter 4.2), E - energy of the particle.

3 Prompt photons production

3.1 Introduction

'Prompt' photons are high transverse energy final state photons which are emitted directly during the hard scattering process. They are of interest for many reasons. First, the photons do not undergo the hadronization processes, which is yet not well known, so the theoretical calculations can be done with better precision. Then, they are easier to detect and measure cleanly than hadronic jets since the photon is the only neutral particle which goes to the detector but not a set of charged particles. Also, the final state photon is a particle which arrives in the detector having taken part in the actual hard scattering process and so can provide direct information on the process and the proton structure.

3.2 Prompt photons at HERA

As with all DIS processes at HERA, two major classes of process can be defined in lowest order QCD, direct and resolved. In case of prompt photon production there are two further subclasses in each process: the non-fragmentation and fragmentation processes. In the non-fragmentation processes a prompt photon is produced directly in the hard scattering, while in the fragmentation processes it is produced via fragmentation of the final state parton. The total prompt photon contribution is denoted as QQ to show the quark radiation and to distinguish from the lepton radiation (LL).

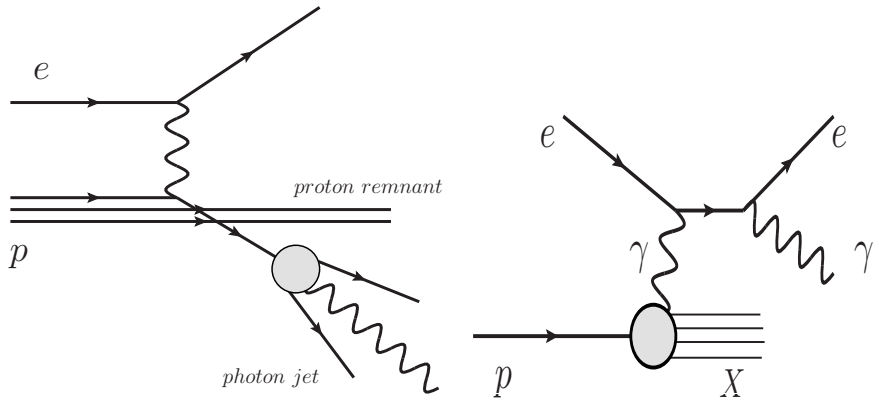

Figure 3.1: Fragmentation (left) and MRST (right) diagrams for the theory calculations in ep collision

The recent theory [2] shows the theoretical predictions up to leading order of $O(\alpha^3)$ including the contributions of LL, QQ, their interference ($LL + QQ$) and the fragmentation $D_{q\to\gamma}$. Another theoretical calculations (MRST, [3]) made for the considering that photon was emitted from the proton. The contribution to the cross section in this case can be expressed as $\gamma_P \otimes \hat{\sigma}(e\gamma \to e\gamma)$, where γ_P denotes the photon structure function in the proton, and $\hat{\sigma}(e\gamma \to e\gamma)$ corresponds to the QED cross section of photon radiation from the quark. Since it has experimental requirements that are not considered in the present analysis, these calculations were not taken into account. The correspondent diagrams are shown in Fig. 3.1.

3.2.1 Direct/resolved non-fragmentation processes

In the kinematic region available at HERA, the direct non-fragmentation process in prompt photon production is dominated by the LO "QCD Compton" process (Figure 3.2)

$$\gamma q^p \rightarrow \gamma q$$

where q^p denotes the quark contents of a proton. An incoming photon interacts with a quark in a proton. There are a high P_T photon and a high P_T jet in the observed final state. This process contributes to the cross section with the order of $O(\alpha_{em}^2)$, where α_{em} is an electromagnetic coupling constant. In the resolved non-fragmentation process, there are three processes (Figure 3.2)

$$q^\gamma g^p \rightarrow \gamma q$$
$$q^\gamma q^p \rightarrow \gamma g$$
$$g^\gamma g^p \rightarrow \gamma q$$

These processes contribute in order of $O(\alpha_{em}\alpha_s)$(hard scattering process) multiplied by the factor $O(\alpha_{em}/\alpha_s)$ for the photon structure and thus has the cross section value of the same order as for the direct processes.

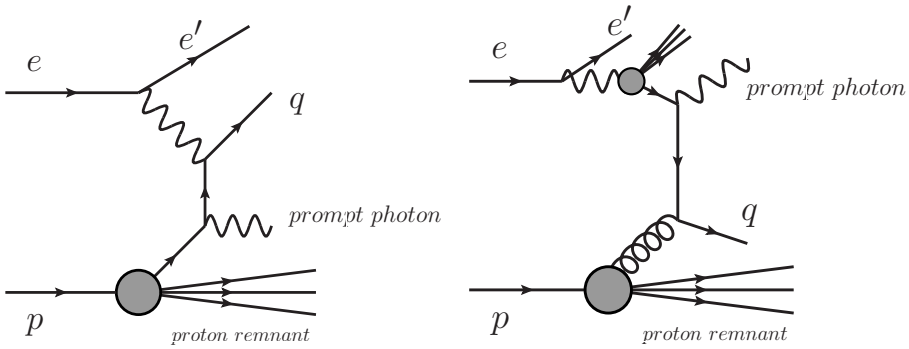

Figure 3.2: Direct (left) and resolved (right) non-fragmentation prompt photon production in ep collision

3.2.2 Direct/resolved fragmentation processes

A prompt photon can also come from the fragmentation of a jet. Thus the diagrams that contribute to the cross section are the same as with the dijet process. The direct and resolved fragmentation processes

$$\gamma q^p \to qg$$
$$q^\gamma g^p \to qg$$

are shown if Fig. 3.3.

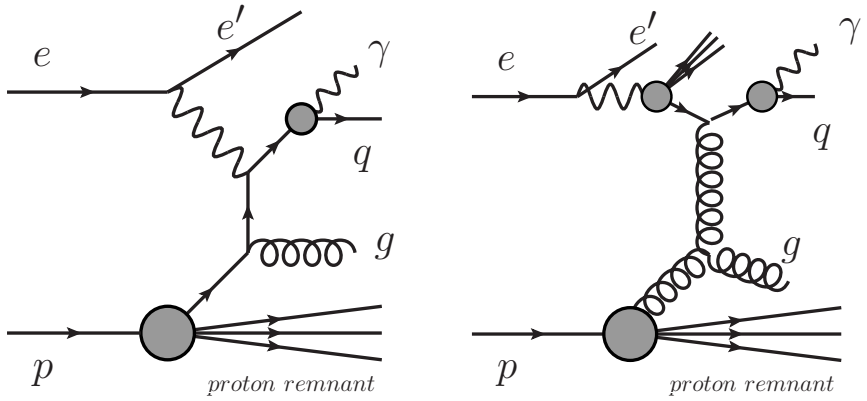

Figure 3.3: Direct (left) and resolved (right) fragmentation prompt photon production in ep collision

If the photon takes almost all the energy of the jet, these photons cannot be distinguished from non-fragmentation photons. The cross section of fragmentation processes strongly depends on the fragmentation functions.

3.3 Background events

Photons identified by the detector as prompt photons can arise from other processes besides that of interest. Some of these photons can be suppressed by selecting appropriate cuts, the others cannot be distinguished and thus the statistical methods need to be applied.

3.3.1 Initial and Final State radiation

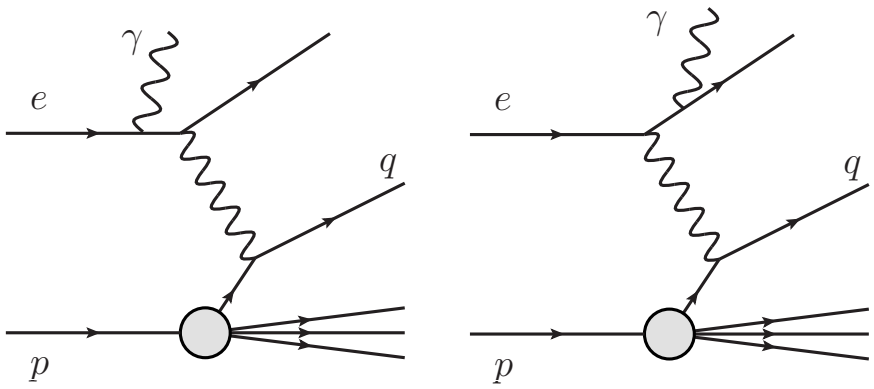

Figure 3.4: Photons produced from incoming electron (left) and scattered electron (right)

In hard scattering processes the photon can be emitted as shown in fig. 3.4. Such processes are called initial and final state radiation. The cross-section of these processes is much higher then prompt photon's ones. This process cannot be suppressed but it is calculated by theory with high precision. In the present work, such photons are also measured.

3.3.2 Neutral mesons decays

Another types of misidentified photons can arise from neutral meson decays to at least two photons, mainly they are π^0 and η mesons. These events cannot be reject completely, but their kinematic characteristics differ from prompt photon's ones.

3.3.3 Compton QED scattering and DVCS

Two further groups of events exist which have an electron and a possibly isolated photon in the final state. These are QED Compton events, shown in Figure 3.5 and Deeply Virtual Compton Scattering, DVCS, shown in Figure 3.6.

Both QED Compton and DVCS events can be easily suppressed by demanding the presence of some hadronic activity in the calorimeter which is absent in Compton scattering and DVCS.

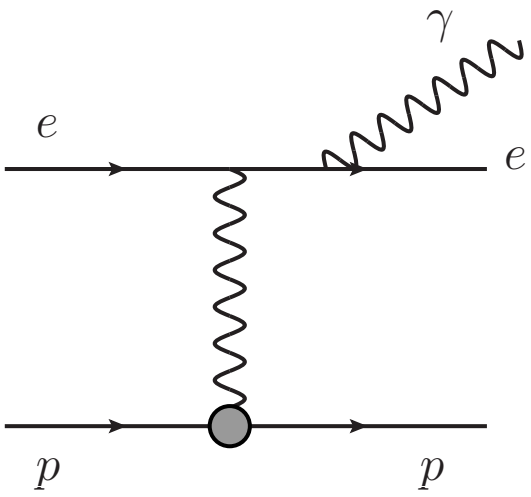

Figure 3.5: Photons production in Compton scattering process

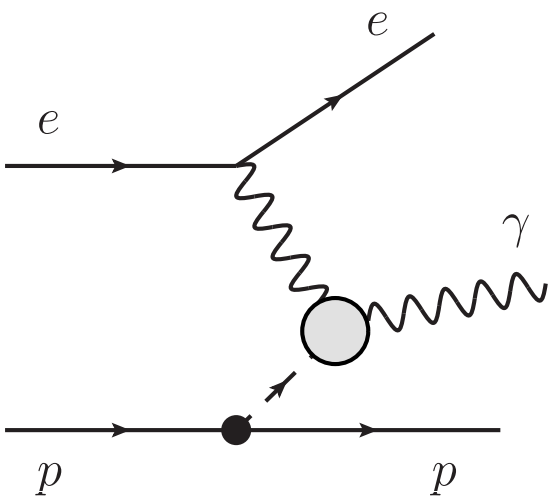

Figure 3.6: Photons production in Deeply Virtual Compton scattering process

3.4 Observations in previous experiments

To be edited.

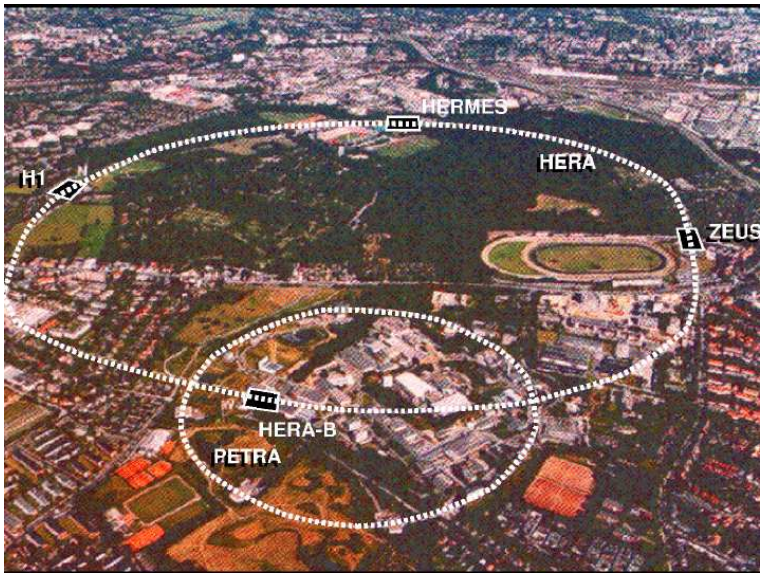

Figure 4.1: HERA accelerator with pre-accelerator PETRA and 4 experimental halls

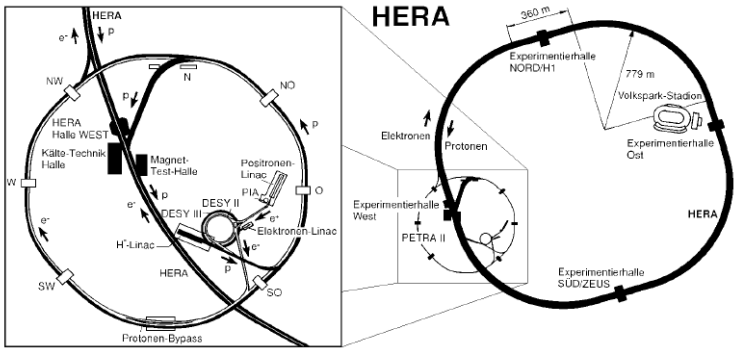

Figure 4.2: Schematic diagram of HERA accelerator; 4 experimental halls and pre-accelerator enlarged

4 HERA and ZEUS description

4.1 HERA

HERA accelerator[2] [1] is the first and the largest electron-proton collider in the world. It is located in DESY[3] site in Hamburg, Germany. HERA was designed to accelerate electrons [4] to the energy of 27.5 GeV and protons to the energy of

[2]Hadron Elektron Ring Anlage

[3]Deutsches Elektronen SYnchrotron

[4]The word electrons is used here to mean either electrons or positrons

820(920[5]) The center of mass energy is $\sqrt{s} = 300(318)$ GeV.

The accelerator was constructed between 1984 and 1990, and measures 6.3km around its circumference. Four separate experiments are located around the ring in four large experimental halls which are at a depth of around 25 meters. There are two experiments studying collider physics, ZEUS [4] and H1 [5] which are situated at the interaction points where the separate lepton and hadron beams are brought together. Two further experiments, HERMES [6], which looks at polarization effects using the lepton beam and a fixed target, and HERA-B [7], which uses the hadron beam to study CP-violation in B meson decay, are also situated on the HERA ring.

The first stage of proton acceleration take place in the linear accelerator where 50 MeV H^- ions are stripped of their charge and injected into DESY III. There they are accelerated to 7.5 GeV and injected into PETRA II. PETRA II can hold up to 70 bunches which are then accelerated to 40 GeV. After this injection to the HERA ring occurs and the protons are accelerated to their final energies of 820(920) GeV.

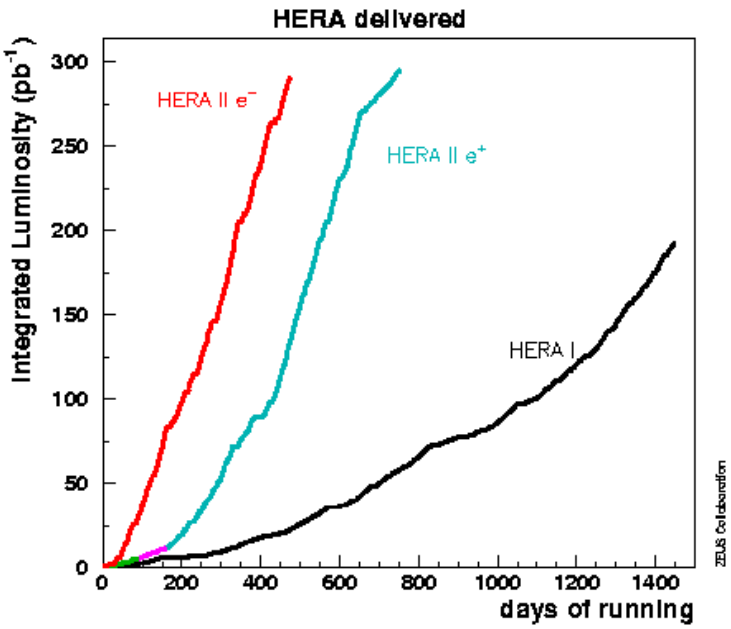

Figure 4.3: Integrated luminosity for both periods (HERA I 1992- 2000, HERA II 2004- 2007)

[5]In 1998 the beam energy was increased to 920 GeV

The injection of electron starts from linear accelerators LINAC I and II where the electrons are accelerated to 220 and 450 MeV respectively. They are then transferred to DESY II synchrotron and are accelerated to 7.5 GeV before transfer to PETRA II. In PETRA II bunches of electrons are collected and accelerated to 14 GeV and then the bunches are finally injected into HERA before being accelerated to their maximum energy of 27.5 GeV.

Electron acceleration is carried out via conventional magnets but proton acceleration is done using superconducting magnets, cooled using liquid helium.

After synchronizing and adjustment procedures the beams collide with the period of 96 ns. Collider provides the luminosity of about $14 \cdot 10^{30} cm^{-2} s^{-1}$. Integrated luminosity for the years 1992-2000 (HERA I) and 2002-2007 (HERA II) in ZEUS experiment are shown at Fig.4.3.

4.2 ZEUS

The ZEUS detector is a large multipurpose detector, designed to study lepton-hadron scattering, and has near 4π coverage in solid angle, except for small regions around the forward and rear beampipes. The ZEUS coordinate system is shown in Fig 4.4. The z axis follows the line of the beam direction. The x and y axes point to the centre of the HERA ring and directly upwards, respectively. The polar angle, θ, is measured with respect to the proton beam direction. The azimuthal angle, ϕ, is measured with respect to the x axis in the $x - y$ plane. Often the quantity pseudorapidity is used instead of θ ($\eta = -ln\left(tg\frac{\theta}{2}\right)$).

Figure 4.5 shows a cross sectional view of the layout of the ZEUS detector in the longitudinal ($z - y$) and transverse ($x - y$) planes with respect to the beam direction, respectively. A brief outline of the detector components is given in the following. The parts of the detector essential for the present analysis are described in more detail in the following sections. A full description of the ZEUS detector is given in [8].

The main parts of the ZEUS detector are as follows.

- Central tracking detector (CTD) [9], aided by an axial magnetic field of

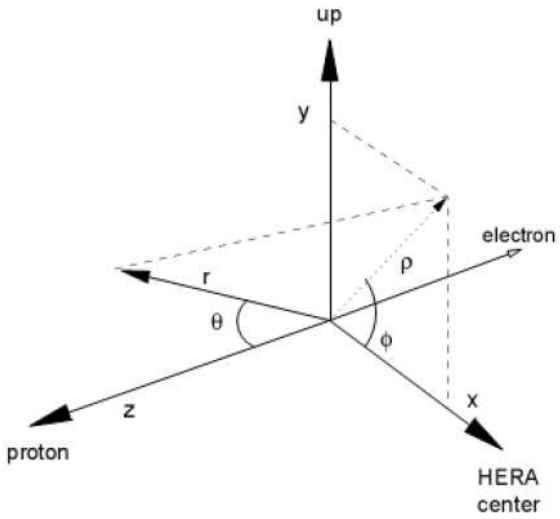

Figure 4.4: ZEUS coordinate system

1.43T;

- Micro vertex detector (MVD), installed in 2000 after the reconstruction. Is used for more precise measurements of track momentums and track reconstruction;
- Uranium scintillator calorimeter (UCAL)[10] which measures with high precision energies and directions of particles and jets;
- Barrel Preshower Detector [11], [12], located between the solenoid and the calorimeter to correct particle energies measured in the calorimeter, and also for separating the particles of different types ($e/\pi^{\pm}$, γ/π);
- Backing calorimeter (BAC) for measuring leaked out of UCAL energy;
- 3-component (forward, barrel and rear) system of muon chambers; 3 inner chambers (FMUI, BMUI, RMUI) and 3 outer (FMUO, BMUO, RMUO);
- Small-angle Rear Tracking Detector (SRTD) which improves the angular resolution on the scattered electron in the rear direction.

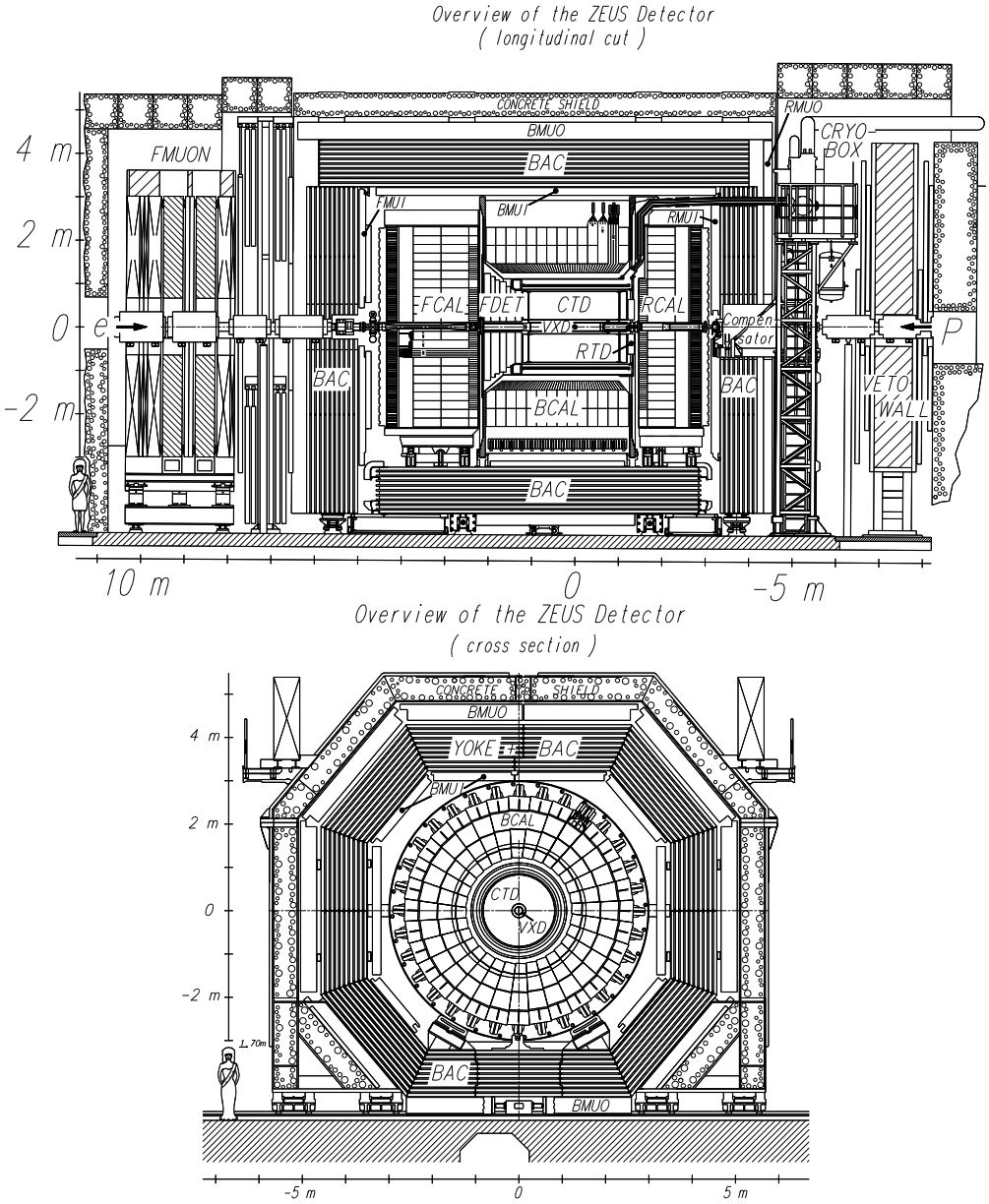

Figure 4.5: A schematic diagram of ZEUS detector in zy and xy plane

4.2.1 UCAL

The main part of the ZEUS detector is the uranium scintillator calorimeter (UCAL)[10] which measures with high precision energies and directions of particles and jets. It has a layered structure and is built from depleted uranium (DU; 98.1% ^{238}U, 0.2% ^{235}U, 1.7% Nb) plates interleaved with plastic scintillator (SCSN38) plates. Readout of the light from the scintillator is achieved by means of plastic wavelength shifters (WLS) with associated photo-multipliers.

The layout of the calorimeter is shown in Fig. 4.5. It consists mechanically of

three independent components: Forward Calorimeter (FCAL), Barrel Calorimeter (BCAL) and Rear Calorimeter (RCAL), covering the polar angle ranges $2^\circ - 40^\circ$, $37^\circ - 129^\circ$ and $128^\circ - 177^\circ$, respectively. It provides solid angle coverage of 99.8% in the forward hemisphere and 99.5% in the backward hemisphere. The depth of the calorimeter was optimized by requiring that 95% of the shower energy is contained for 90% of the jets of maximum possible energy from the HERA kinematics which falls from 800 GeV at the forward proton direction ($\theta = 0^\circ$), to about 300 GeV at $\theta = 30^\circ$, 100 GeV at $\theta = 60^\circ$ and less than 50 GeV for $\theta \geq 90^\circ$.

The UCAL has a modular structure. Each FCAL/RCAL module has a width of 20 cm, an active depth up to 1.53 m and a height for the active part varying from 2.2 to 4.6 m, depending on its position with respect to the beam. The modular structure of BCAL constructed from 32 identical modules each covering an angle wedge of 11.25° in ϕ with a length of 3.3 m in the beam direction. All modules are tilted by 2.5° to avoid particles from the interaction point travelling through module boundaries.

The FCAL/RCAL modules have a non-projective tower structure. The cell readout in the transverse direction is made in terms of towers of $20 \times 20cm^2$ for HAC sections of both FCAL and RCAL. The EMC sections are further segmented into $5 \times 20cm^2$ and $10 \times 20cm^2$ sections for FCAL and RCAL respectively. As an example of the construction geometry of the calorimeter, 4.6 illustrates the internal structure of an FCAL module. It is made up of layers of 3.3 mm thick DU plates yielding 1 X_0 of sampling thickness for both EMC and HAC and 2.6 mm thick SCSN-38 scintillator plates. The thickness of the uranium and scintillator plates was optimized to achieve an equal response of the calorimeter to electrons and hadrons (compensation; $e/h = 1$).

The UCAL is compensating with an electromagnetic energy resolution of $18\%/\sqrt{E} \oplus 1\%$ (GeV) and a hadronic energy resolution of $35\%/\sqrt{E} \oplus 2\%$(GeV). The calorimeter response to electrons is linear within $\pm 2\%$ up to 110 GeV/c. The angular resolution for the scattered electron is better than 10 mrad. In addition the UCAL provides excellent timing, better than 1.5 ns compared to the HERA bunch crossing time of 96 ns, which has played a crucial role in the fast rejection of beam gas background from the physics samples.

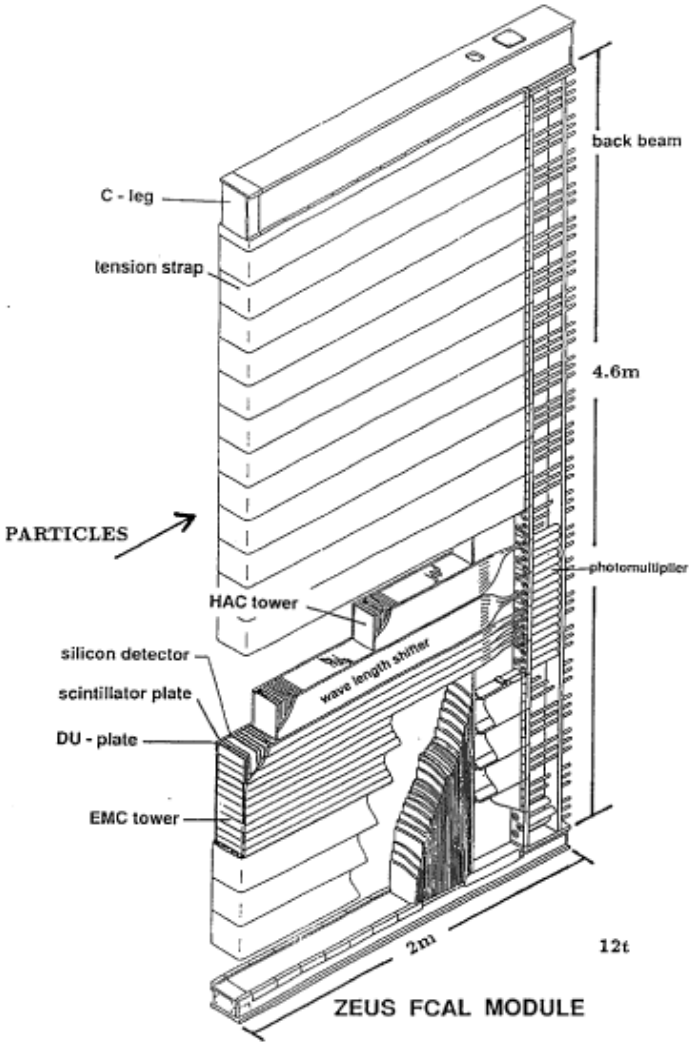

Figure 4.6: Internal structure of a FCAL module. The $20 \times 20 cm^2$ towers with their longitudinal division into EMC and HAC section are shown

4.2.2 CTD

The central tracking detector (CTD) [9] measures the direction and momentum of charged particles with high precision and estimates the energy loss dE/dx used for particle identification. The CTD is a cylindrical drift chamber with an inner radius of 18.2 cm, outer radius 79.4 cm and length of 205 cm, filled with a gas mixture of 90% argon, 8% CO2 and 2% ethane. It covers a polar angle of 15° to 164° and consists of 72 radial layers, organized into 9 superlayers.

Figure 4.7 shows the wire layout in a single octant of the CTD. Alternating layers of sense and field wires are indicate by the dots. The larger dots are the

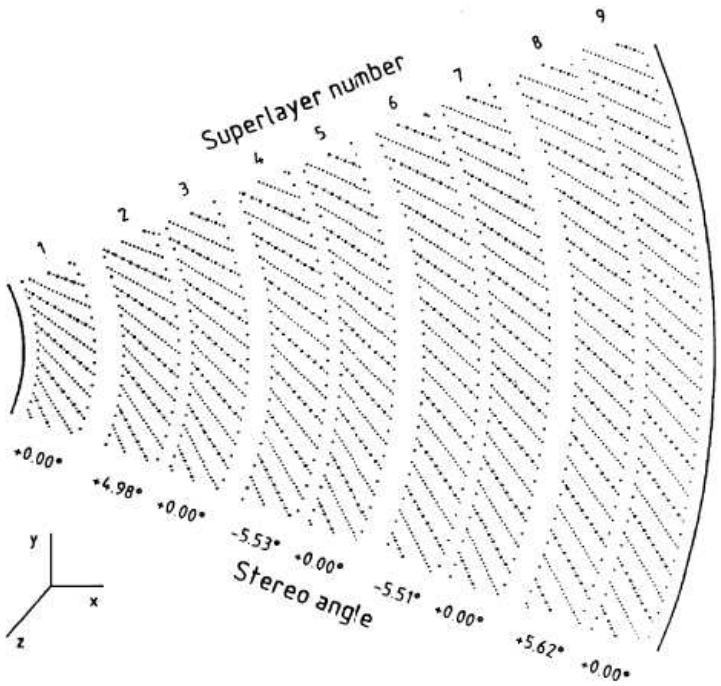

Figure 4.7: Schematic diagram of one octant of the CTD

sense wires. The odd superlayers are axial layers which have sense wires parallel to the beam axis, while the even superlayers are stereo layers, inclined at angle $\pm 5^\circ$ with respect to the beam axis, which allows the determination of the z-position of the hits. For trigger purpose, the inner three axial layers are additionally equipped with a z-by-timing system ($\sigma_z \sim 4cm$) which determines z-position of a hit from the difference in arrival times of a pulse at both ends of the chamber. The nominal resolution of the CTD was per hit around $180\mu m$-$190\mu m$ in $r - \phi$, resulting in a transverse momentum resolution of $0.005 p_T \pm 0.0016$ for long tracks (> 3 superlayers). The z-vertex resolution for medium and high multiplicity events, taken from many track measurements, is < 1.5 mm.

4.2.3 LUMI monitor

The luminosity at HERA is measured via the rate of the bremsstrahlung process $ep \rightarrow ep\gamma$. The luminosity monitor (LUMI) consists of two separate detectors; one of which measures the scattered electron and the other the photon.

The layout of luminosity monitor is shown in Fig. 4.8.

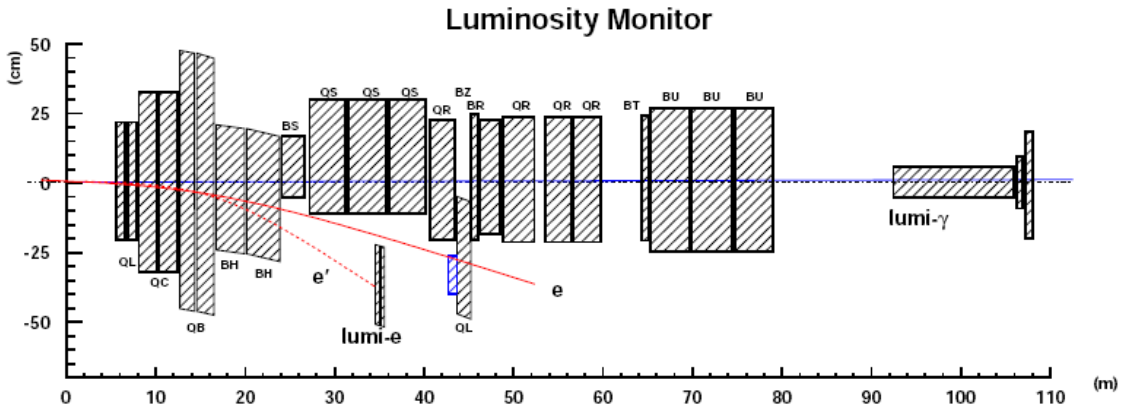

Figure 4.8: The luminosity monitor

A lead-scintillator sampling electron calorimeter, situated 35 m from the interaction point in the electron direction, measures the energy of electrons scattered at small angle to the beam direction. It detects electrons with $\theta'_e < 6$ mrad with an efficiency greater than 70% for $0.35E_e < E'_e < 0.65E_e$.

A photon detector is located close to the proton beam 107 m downstream of the interaction point in the direction of the electron beam. A carbon filter is used to absorb synchrotron radiation, a Cherenkov counter vetos charged particles and finally a lead-scintillator sampling calorimeter measures the energy of the photon. The geometrical acceptance is 98% for the process $ep \to ep\gamma$ and is independent of the energy of the photon. The value of the integrated luminosity was measured to an accuracy of $\pm 2.5\%$.

5 Data acquisition system and analysis framework

The short bunch crossing time at HERA of 96 ns, equivalent to a nominal rate of $\sim$ 10 MHz, is a technical challenge which puts stringent requirements upon both the ZEUS Trigger and the Data Acquisition (DAQ) system. The total interaction rate, which is dominated by background from upstream interactions of the proton beam with residual gas in the beam pipe, is of the order 10-100 kHz while the rate of ep physics events in the ZEUS detector is of the order of a few Hz. Other background sources are electron beam gas collisions, beam halo and cosmic ray events.

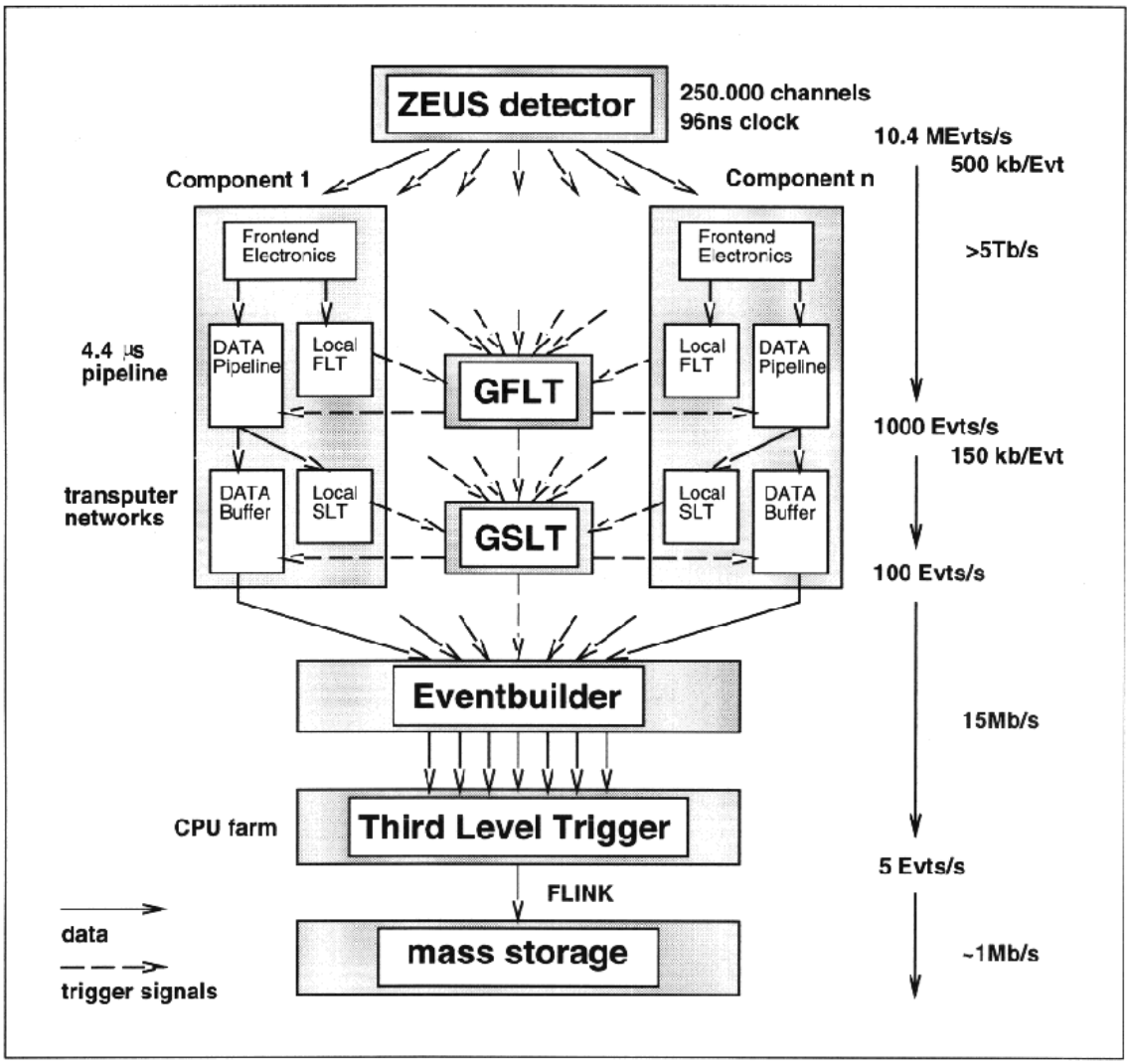

Figure 5.1: Data acquisition system and data processing in ZEUS

ZEUS employed a sophisticated three-level trigger system in order to select ep physics events efficiently while reducing the rate to a few Hz. A schematic overview of the ZEUS trigger system is shown in figure 5.1. The First Level Trigger (FLT) is a hardware trigger, designed to reduce the input rate below 1 kHz. Each detector component has its own FLT, which stores the data in a pipeline, and makes a trigger decision within 2 μs after the bunch crossing. The decision from the local FLTs are passed to the Global First Level Trigger (GFLT), which decides whether to accept or reject the event, and returns this decision to the component readout within 4.4μs.

If the event is accepted, the data are transferred to the Second Level Trigger (SLT), which is software-based and runs on a network of Transputers. It is de-

signed to reduce the rate below 100 Hz. Each component can also have its own SLT, which passes a trigger decision to the Global Second Level Trigger (GSLT). The GSLT decides then on accepting or rejecting the event.

If the event is accepted by the GSLT, all detector components send their data to the Event Builder, which produces an event structure on which the Third Level Trigger (TLT) code runs. The TLT is software based and runs part of the offline reconstruction code on a farm of Silicon Graphics CPUs. It is designed to reduce the rate to a few Hz. Events accepted by the TLT are written to tape via a fiber-link (FLINK) connection. The size of an event is typically 100 kBytes. From here on events are available for full offline reconstruction and data analysis.

Further data processing is done with ORANGE [13] program, that provides reading of the data and convert this information to the outer format that is comfortable to use. Also ORANGE provides a possibility to choose only useful events, e.g. by analyzing kinematic parameters or the particles of interest. It is very useful, as it reduces the size of output files very significantly.

ORANGE's output is ROOT-based format files. These files are processed using the ROOT framework [14], developed for high energy physics. It provides very wide spectrum of utilities and sub-programs, e.g. filling and fitting histograms, minimization packages etc.

One of the main parts of the analysis is based on using Monte Carlo samples. These samples are generated by the physics event generator (like PYTHIA, ARIADNE). At this stage the final-state particles are generated and then their penetration through the detector is simulated. ZEUS detector simulation is called MOZART and based on GEANT 3 program. This program simulates every final state particle going through the detector.

The main advantage of using Monte Carlo samples is that there also a so-called "TRUE" information is provided. This data contains all information about the particles which were generated: 4-momenta, mother particle, decay particle, lifetime, the place of decay etc. Later on one can compare the TRUE information with its detector measurements and make corrections. If the TRUE information is fully compatible with measured by the detector parameters, we say that the detector is very well simulated. In case these parameters do not correlate, we say

that we need acceptance correction to correctly measure the cross section.

6 Event selection

The event selection used in the present analysis can be divided in two parts. One of them, called cleaning cuts, is used to suppress background events as much as possible. But for making cleaning cuts one should be aware not to reduce statistics too much. Some cleaning cuts are used to reject events of no interest; others are applied to reduce background with a factor which is much higher than for interest events. Another part of the event selection is called phase space cuts. These cuts are used to determine the kinematic parameters for the event. In general, cleaning cuts cannot be translated to theory, and thus are used to decrease statistical error as much as possible.

6.1 DIS event selection

6.1.1 Z vertex

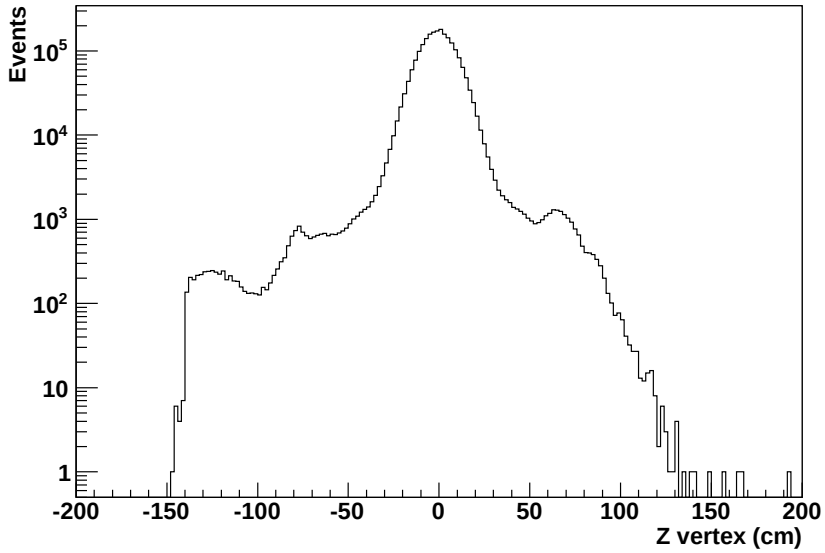

Figure 6.1: z-vertex of the event

The initial event selection involves cuts to select good quality physics events,

by suppressing the large background of non-physics events which occur in ZEUS. Background events are all those arising from processes other than electron-proton scattering, such as beam gas or cosmic ray interactions. The primary signature of electron-proton scattering is a well-defined vertex located within a specified distance of the nominal interaction point (0; 0; 0). The Z_{vertex} distribution before applying cuts is shown in Fig. 6.1. Long tail corresponds to background events. The cut $-40cm < z_{vtx} < 40cm$ was applied in the present analysis.

6.1.2 $\Sigma\,(E - p_z)$

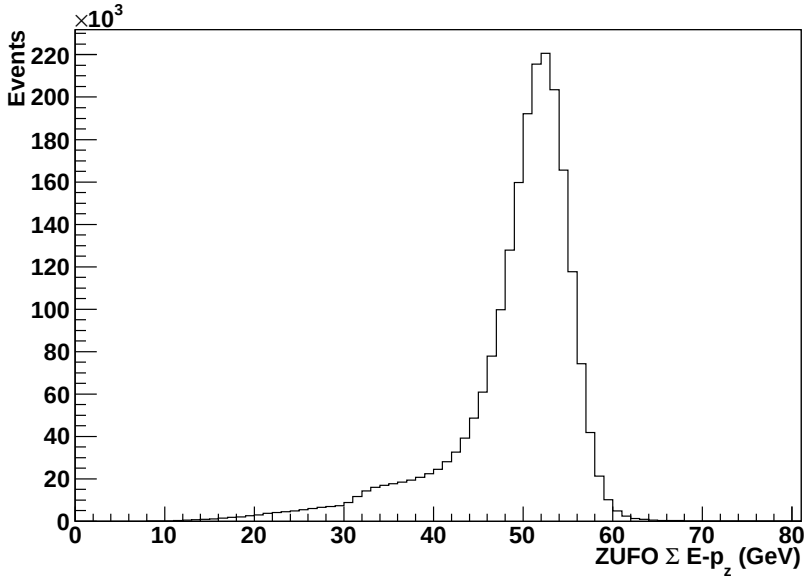

Figure 6.2: $\Sigma\,(E - p_z)$

Value of $\Sigma\,(E - p_z)$ for deep inelastic region ($Q^2 > 10GeV^2$) is $\Sigma\,(E - p_z) = 2E_e = 55GeV$, twice the initial energy of the electron. For the photoproductin events ($Q^2 \sim 0GeV^2$), where the electron escapes undetected, $\Sigma\,(E - p_z) = E_e = 27.5GeV$. The number of photoproduction events is much more than deep inelastic ones. Cutting on $\Sigma\,(E - p_z)$ is very efficient for selecting only DIS events. An upper cut is also applied to exclude events with double interactions occuring. The value of $\Sigma\,(E - p_z)$ is calculated by summing all EFO objects (ZUFOs). $\Sigma\,(E - p_z)$ distribution for DIS before applying cuts is shown in Fig. 6.2.

6.2 Scattered electron finding

Scattered electron is found using the electron finding algorithm SINISTRA95 which is neural network trained. The cuts were applied for the kinematic parameters of the scattered electron:

- $140^o < \theta_e < 172^o$ - polar angle (electron is found in the RCAL, see Fig. 6.3);
- $E_e > 10GeV$ - electron energy in the calorimeter (correspond to the optimal reconstruction efficiency of the scattered electron, see Fig. 6.3).
- So-called "box cut". $|x_e| < 14.8$cm, $-14.6 < y_e < 12.5$cm. This cut corresponds to the possibility that electron goes very close to the beam pipe and thus cannot be detected. In another words, if the electron was detected in this region, this is 'fake' electron and should not be considered.

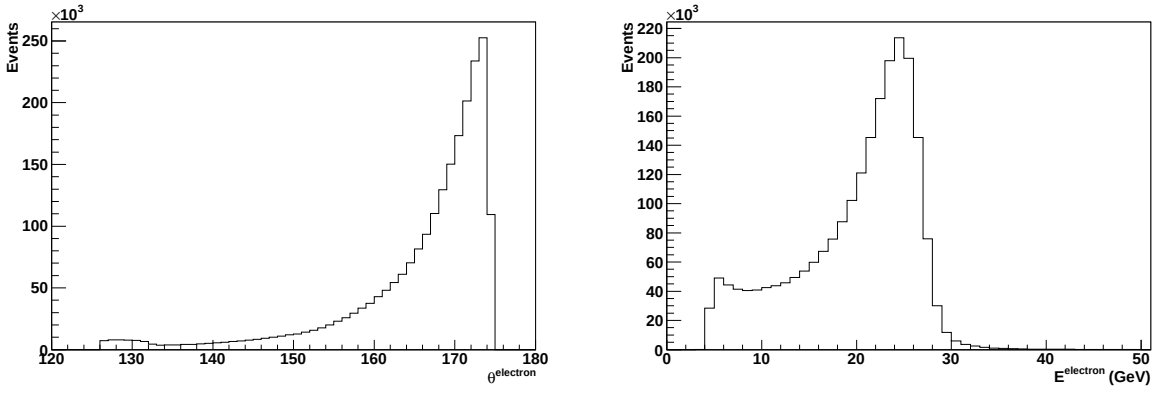

Figure 6.3: θ_e - polar angle of the scattered electron (left) and energy of the scattered electron (right)

To select DIS events the cut on Q^2 measured using the scattered electron was applied : $10 < Q^2 < 350$ GeV^2. Here Q^2 is defined from the initial and final state lepton: $Q^2 = -q^2 = -(k - k')^2$. This value was decreased from 35 Gev^2 since previous measurements [15]. To suppress the fraction of DVCS and Compton scattering events the limitation of the number of vertex tracks not in RCAL was applied: $N_{vertex\ tracks\ not\ in\ RCAL} \geq 2$ (see Fig. 6.4).

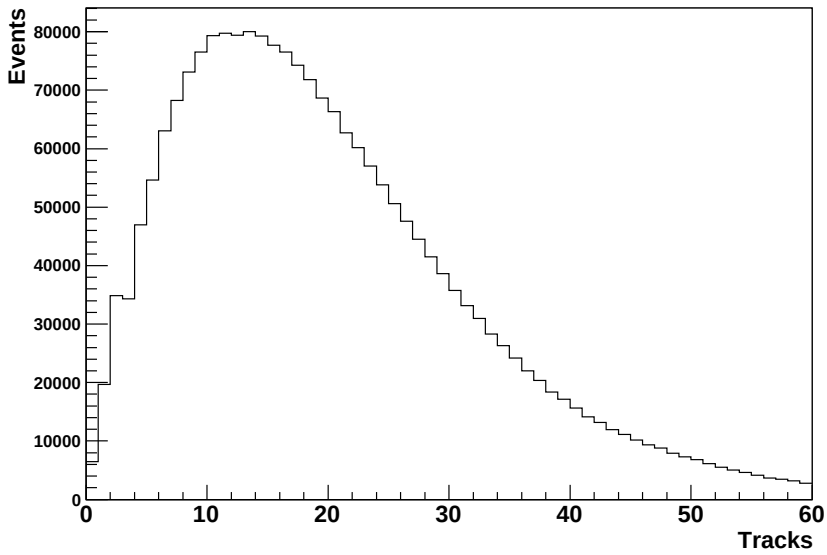

Figure 6.4: The number of tracks in events

6.3 Prompt photon selections

Prompt photons are found using the energy flow objects (EFOs) in the calorimeter, ZUFOs. It uses the information from the calorimeter cells and tracks. There are several types of ZUFOs in ZEUS. In the present analysis only trackless ZUFOs are considered as the photon candidates. Such cuts were applied to the prompt photon candidates:

- $44^o < \theta_\gamma < 127^o \, (-0.7 < \eta_\gamma < 0.9)$ for rejecting photons not in the BCAL.
- $4 < E_\gamma < 15GeV$ for rejecting background events. This region is typical for prompt photons ([16]).
- no tracks corresponds to photon candidate within a cone $\Delta r = \sqrt{(\phi_{tr} - \phi_\gamma)^2 + (\eta_{tr} - \eta_\gamma)^2} < 0.2$, where tr and γ indices correspond to the track and photon candidate. This cut rejects all charged particles that was misidentified as photons.
- $\frac{E_{EMC}}{E_{HAC}+E_{EMC}} > 0.9$ - energy fraction in the electromagnetic part of the calorimeter to the energy of the photon.
- $\frac{E_\gamma}{E_{jet \ containing \ \gamma}} > 0.9$ - energy fraction of the photon candidates to the energy

of the jet containing the photon. This cut is applied to select the photons from jet fragmentation.

7 Jet reconstruction and selection

Jets are the object of interest because of their presence in almost all hard processes. Thus, all quarks are being hadronized and form jets. Measuring their kinematic parameters, we can get these parameters for quarks. Observing the third jet in the event said the physicians about the presence of gluon in 1979. The constant of strong interaction, α_s, can be measured using jets. To look at jets, first we need the definition of the jet.

7.1 Jet definition

A jet is not fundamental QCD object and it is necessary to find an exact definition. Jets are the objects which are observed in hadronic final state events. It is closely corresponds to the kinematics of the final state partons produced in the interaction. Jets are the directly connected to quark and gluon activity, but since the latter are not observed it is the only way to measure parton's features. The easiest definition, probably, is the set of particles going close to each other and having similar energies.

In order to unify the theoretical predictions and experimental observes of jets, the Snowmass Workshop [17] stated in 1990 that any jet definition should be simple to implement in an experimental analysis and in theoretical calculations, should be defined at any order of perturbation theory, and should yield a finite cross section at any order of perturbation theory that is also relatively insensitive to hadronization.

Experimentally, hadron jets can be reconstructed by any reconstruction program which uses as input the information from the calorimeter and tracks. All programs have similar algorithms and thus have the same results. In the present work the following programs were compared:

- KTCLUS algorithm as a part of ORANGE software.

- KTJET program [18].
- fastjet program [19].

On the experimental side, jets are found by any jet finding algorithm and then are reconstructed using information from the calorimeter and/or tracks from tracking detector. In the theoretical calculations, jets can be found as the set of particles after the hard processes (parton level jets) or after hadronization process using final state particles (hadron jets). It is necessary to have good correspondence between jets at all levels. Also an important aspect is that the jet definition for experimental and theoretical quantities should be consistent.

7.2 Jet finding algorithm

Mainly there are two jet finding algorithms, which search for jets. They are the cone algorithm in accordance to the Showmass Convention and k_T clustering algorithm which combines objects with small relative transverse energy into jets.

Cone algorithm is looking for particles that fly close to each other. The arbitrary first particle is matched to the arbitrary second particle and if the distance $\Delta R = \sqrt{\Delta\eta^2 + \Delta\phi^2}$ between them is rather small (depending on the chosen parameter R_0 the new particle is reconstructed from these two. Then another particle is considered. The same procedure is repeated until all particles form jets.

The k_T clustering algorithm work in a bit different way. It depends on a chosen parameter, R. To decide which particles should be merged, for each particle i we form the quantity, $d_i = E_{T,i}^2$ and for each pair of particles, ij , we form the quantity

$$d_{ij} = min(E_{T,i}^2, E_{T,j}^2)[(\eta_i - \eta_j)^2 + (\phi_i - \phi_j)^2]/R^2$$

The d_i is the limiting case of small angles of the "distance" between particle i and a large mass remnant travelling along the z direction. If the smallest of all the d values is a d_{ij}, the particles i and j are merged into a single object, k. If however, the smallest value is a d_i then this particle is considered "complete" and is removed from further clustering. This process is then repeated until all the

objects have been removed, producing an E_T ordered list of objects. In the present analysis the implementation of k_T clustering algorithm to ORANGE software was used with the radius parameter of $R = 1.0$. Also the offline implementation of K_T jet [18] algorithm was used to match jets and correct jet energy.

7.3 Jet transverse energy correction

The ZEUS detector is known to be underestimating jet energy due to some dead material that is not taken into account during the analysis procedure. To measure correctly the energy of jets, the procedure of correction is applied for every jet. This procedure is based on Monte Carlo samples. The detector level jet energy corresponds to some hadron level jet energy. To get this correspondence jets are matched

7.3.1 Data samples for the correction

Only detector level jet energy in Monte Carlo and also data jet energy are corrected according to the correction value. Positron and electron data are corrected separately using ARIADNE correction values. Data periods 040607 of positrons are corrected using 0607 positron ARIADNE sample, data periods 040506 of electrons are corrected using 040506 electron ARIADNE samples. The signal Monte Carlo (PYTHIA) is corrected using it's own correction value as it differs from ARIADNE's one much.

7.3.2 The procedure of the correction

The procedure of correction is as follows.

1. Cluster all ZUFOs and TRUE particles excluding DIS electron candidate to jets.

2. In each event choose the only closest pair of hadron and detector level jets. The distance between jets is defined as $\Delta R = \sqrt{\Delta\eta^2 + \Delta\phi^2}$. If the minimal distance is greater than 0.5 the event is skipped. Jet with prompt photon candidate is not taken into account.

3. Fill $2D$ histogram $E_{T,jet}^{Detector}$ vs $E_{T,jet}^{Hadron}$ for these pairs for 11 bins of $-1.5 < \eta_{jet}^{Hadron} < 1.8$.

4. In each bin of 0.5 GeV of $E_{T,jet}^{Hadron}$ the distribution $E_{T,jet}^{Detector}$ is fitted to Gaussian by χ^2 minimization to determine the correspondence $E_{T,jet}^{Hadron}$ to $E_{T,jet}^{Detector}$.

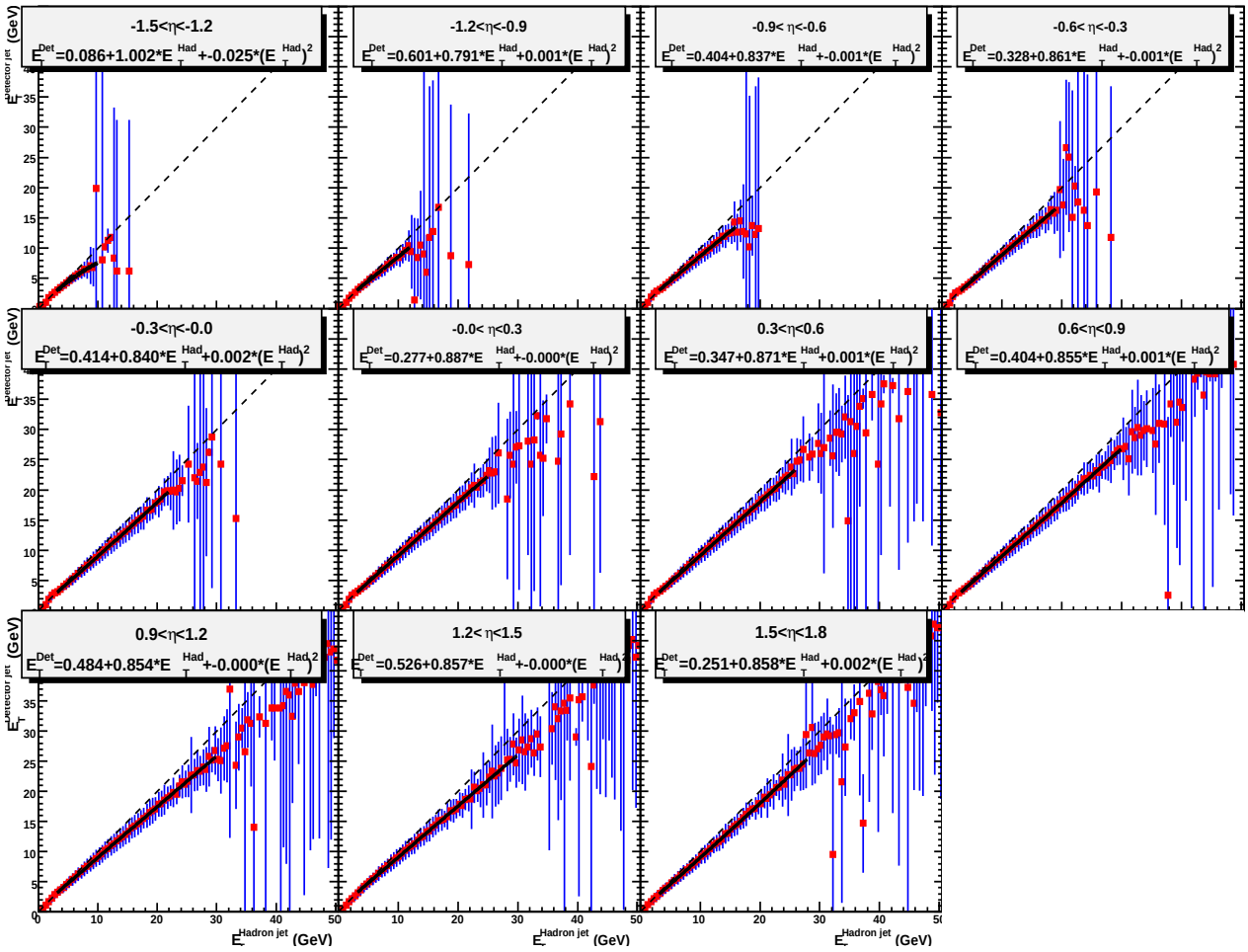

Figure 7.1: Uncorrected transverse energy in the laboratory frame of the detector-level jets $E_{T,lab}^{det}$ in 11 η_{lab} regions. The points are the mean values of Gauss functions which are fitted in each $E_{T,lab}^{had}$ bin, the errors bars give their standard deviation. The dashed line shows the function $E_{T,lab}^{det} = E_{T,lab}^{had}$. The solid line shows the fit function within fitting ranges.

5. Plot measured values as $2D$ plot with errors equal to standard deviation.

6. Fit this plot to 2nd degree polynomial within reasonable ranges and get the

dependence $E_{T,jet}^{Detector} = P_0 + P_1 \cdot E_{T,jet}^{Hadron} + P_2 \cdot (E_{T,jet}^{Hadron})^2$. The second degree polynomial function was decided to use because of better description of the shape. The criterion that the fit is good is p-value more than 0.1. P-value is calculated as $\int_{q_\nu,obs}^{\infty} f_{\chi^2}(z; NDF)dz$, where $q = -2ln\lambda(\nu)$ and λ is the likelihood of the fit. For first degree polynomial function the p-value was much less (of order 10^{-6}, for second degree polynomial the p-value is almost 1. The fit for ARIADNE positron sample is shown on Fig. 7.1

7. The correction formula is the inverse dependence $E_{T,jet}^{Corrected} = \frac{-P_1+\sqrt{P_1^2-4P_2\cdot(P_0-E_{T,jet}^{Hadron})}}{2P_2}$.

8 Evaluation of the photon signal

After event selection described in chapter 6, final event sample consist of real prompt photons with high transverse energy, and also of a background that consist of neutral mesons decay products (π^0 and η) and electron radiation. For the signal extraction statistical method of background subtraction is used (see Chapter 8.3). In this method different Monte Carlo samples are used.

8.1 Data samples

For prompt photons analysis several data and Monte Carlo samples are required. In the present analysis such samples were used:

1. Data taken by the ZEUS detector in the period from 2004 to 2007 years. The data include electron-proton and positron-proton (depending on the period) collision events. Integral luminosity is 320 pb^{-1}. The sample is called "DATA".

2. Monte Carlo ARIADNE 4.12 sample which include electron- and positron-proton collision events. Integrated luminosity is 460 pb^{-1}. In this sample almost all known particles are simulated. It does not include prompt photons. This sample is divided into two subsamples for different purposes:

(a) High transverse energy lepton radiation sample ("LL" - lepton radiation). As lepton radiation is predicted by QED with high precision this sample is used with fixed ratio scaled by the luminosity.

(b) Hadronic decays etc. (everything without lepton radiation, "background"). This sample is not fixed and used together with the next sample.

3. Monte Carlo PYTHIA 6.416 ([20]) sample with prompt photons ("QQ" - quark radiation). Also it is called "signal". It is used with the "background" to measure statistically the number of prompt photons in the real data events.

8.2 Neutral mesons decays

After making cuts to suppress the contribution from other leading order photon producing processes the major background to the analysis is misidentification of final state neutral mesons, η and π^0, as photons. The decay processes which contribute to the background found are listed below:

$\pi^0 \to \gamma\gamma$	$(98.798 \pm 0.032\%)$
$\eta \to \gamma\gamma$	$(39.31 \pm 0.20\%)$
$\eta \to \pi^0\pi^0\pi^0$	$(32.56 \pm 0.23\%)$

8.3 Signal evaluation methods

For evaluating the number of prompt photons in the real data in selected kinematic region several methods are used. In the present analysis the fit of shower shapes is used. Shower shapes are the characteristics of the photon candidate in the calorimeter. The main shower shapes variables are:

- non-dimensional f_{max} - the ratio of energy in the highest energy cell of a cluster to the total energy of the cluster;
- non-dimensional $\langle \delta z \rangle = \frac{\Sigma(z_i - \langle z \rangle) \cdot E_i}{\Sigma E_i}$ - the energy weighted mean width of the electromagnetic cluster in Z direction.

Both of them represent the width of the electromagnetic shower. The shower produced by different particles look different. For photons from different sources (quark radiation, hadronic decays) are shown in Fig. 8.1.

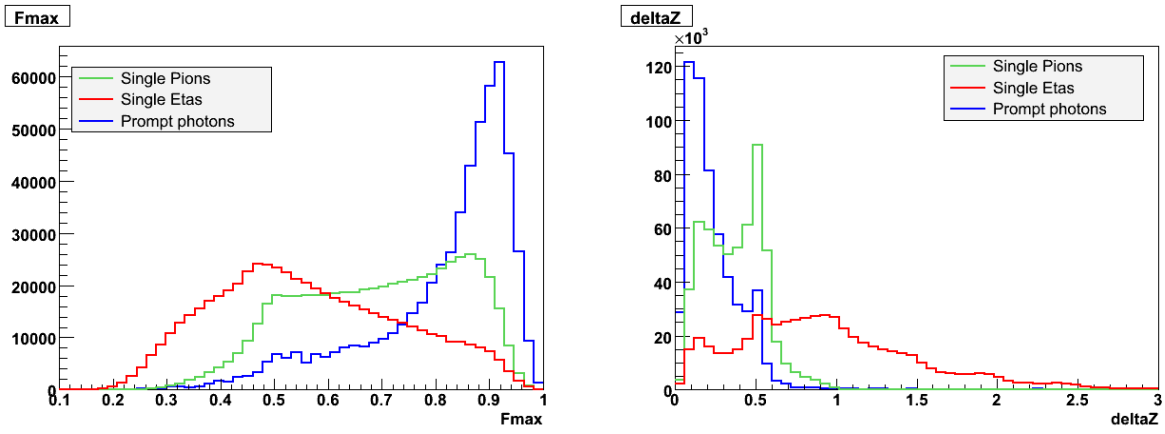

Figure 8.1: Shower shapes from different particles: π^0, η and prompt photons. Area normalized

As is seen from the figures, the shapes are different and data is the sum of all distributions with correspondent weights. This is the key for determining the number of prompt photons in the data. The procedure of measuring this number is as follows. First, all distributions of Monte Carlo are normalized by the number of entries in (data-LL) distribution. The LL Monte Carlo is normalized by the luminosity and afterwards is fixed. Then, we assume that data distribution should be the sum:

$$Data = LL + \alpha \cdot QQ + \beta \cdot Background$$

.

As previously QQ and background were normalized to the number of entries in $(Data - LL)$ subtracted distribution, so $\beta = 1 - \alpha$. After the procedure of normalization we use MINUIT [21] package to determine α parameter by χ^2 method which is defined as [22]

$$\chi^2 = \sum_{i=0}^{b} \frac{\left(D_i - LL_i - \alpha QQ_i - (1-\alpha)\, B_i\right)^2}{\sigma_{D_i}^2 + \sigma_{LL_i}^2 + \alpha^2 \sigma_{QQ_i}^2 + (1-\alpha)^2 \sigma_{B_i}^2}$$

where the sum is over bins within reasonable range of histograms. For the $\langle \delta Z \rangle$ distribution it is necessary to fit not only the photon peak range, but also the background range to be sure that Monte Carlo well describe the data distribution. The fitting range was selected to be $0 < \langle \delta Z \rangle < 0.8$. This makes the shape describe both the photon peak at 0 and pion peak at 0.5. After this procedure the number of prompt photons in the real data is $N_{Prompt\ photons} = \alpha \cdot N_{QQ}$, where $N_{Prompt\ photons}$ is the real number of prompt photons, N_{QQ} is the number of identified photon candidates in the Monte Carlo sample.

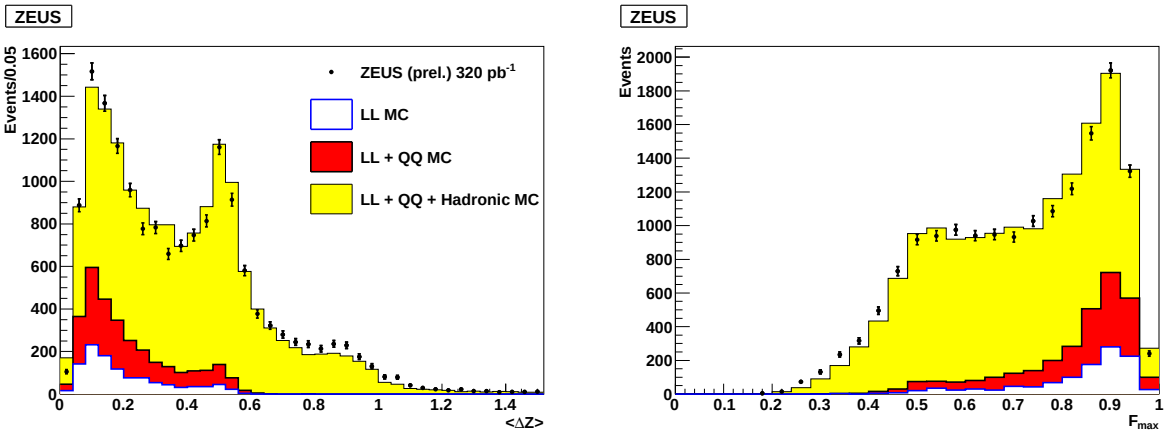

Figure 8.2: $\langle \delta Z \rangle$(left) and f_{max}(right) distributions

The fitting results are shown in Fig.8.2 (the fit on $\langle \delta Z \rangle$, f_{max} distribution is shown for cross-check). The number of found prompt photons is 3101 and the number of radiative photons is 1113.

9 Inclusive Prompt Photon Production

The distributions of photons from different origins are shown in Fig. 9.1.

The kinematic characteristics of the photons from different sources differ and it point us that the physics is different for these events.

The differential cross-section as a function of some observable P is calculated

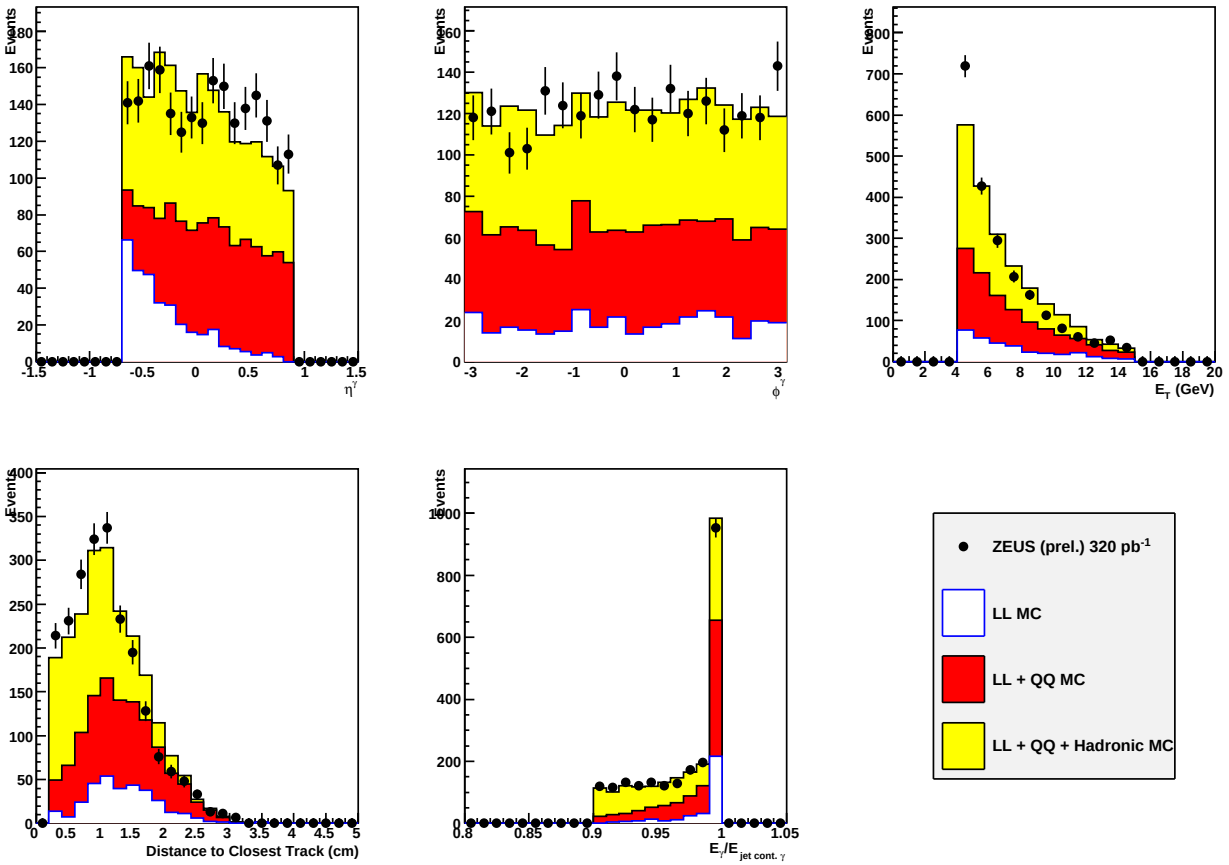

Figure 9.1: Distributions of photon variables: pseudorapidity, phi, transverse energy, distance to the closest track, fraction of the photon energy to the energy of the jet containing photon

according to the formula 9.1

$$\frac{d\sigma}{dP} = \frac{N(P)}{A(P) \cdot \Gamma(P) \cdot \int \mathcal{L} dt} \tag{9.1}$$

where $N(P)$ is the number of events measured in correspondent bin. $A(P)$ is acceptance (see chapt. 9.2), $\int \mathcal{L} dt$ =320 pb^{-1} is the integrated luminosity of the data analyzed. $\Gamma(P)$ comes from dividing by bin-width.

9.1 Efficiency, purity

The bin efficiency is defined as

$$Efficiency(i) = \frac{\#\ of\ Event\ generated\ \&\ reconstructed\ in\ bin\ i}{\#\ of\ Event\ generated\ in\ a\ bin\ i}$$

and is interest since it gives the fraction of the 'true' hadron level particles that was reconstructed in the same bin to the number of generated particles. The higher the efficiency, the greater the fraction of hadron level measured by the detector.

The bin purity is defined as

$$Purity(i) = \frac{\#\ of\ Event\ generated\ \&\ reconstructed\ in\ bin\ i}{\#\ of\ Event\ reconstructed\ in\ a\ bin\ i}$$

and gives the fraction of the events that were reconstructed experimentally and actually which have correspondent hadron level particle in the same bin of the distribution. High purities indicate that the contamination of the sample from events migrating from other bins is small. Both efficiency and purity are calculated using the signal PYTHIA Monte Carlo sample. The ideal values are 1 and this means that we understand the detector absolutely correctly. Usually the values of 50-80% are good. In some analyses these values can be less than 10% and this can be explained by the difficulties of registering those particles and/or high background.

9.2 Acceptance

Acceptance variable shows how good is the detector understanding of the process. The ideal acceptance value is 1. This means that detector "catch" all particles that was generated by Monte Carlo programs. If the acceptance is low it means that the detector underestimate the number of particles. If the acceptance is high (more than 100%) it means that detector register a lot of fake signals. In the present inclusive prompt photons analysis usual value of the acceptance is 70-80%. Acceptance is calculated using PYTHIA Monte Carlo sample according to the formula 9.1.

$$A(P) = \frac{N_\gamma^{reco}}{N_\gamma^{true}} \tag{9.1}$$

where N_γ^{reco} is the number of reconstructed events in the according P bin, N_γ^{true} is the number of generated events in the according bin.

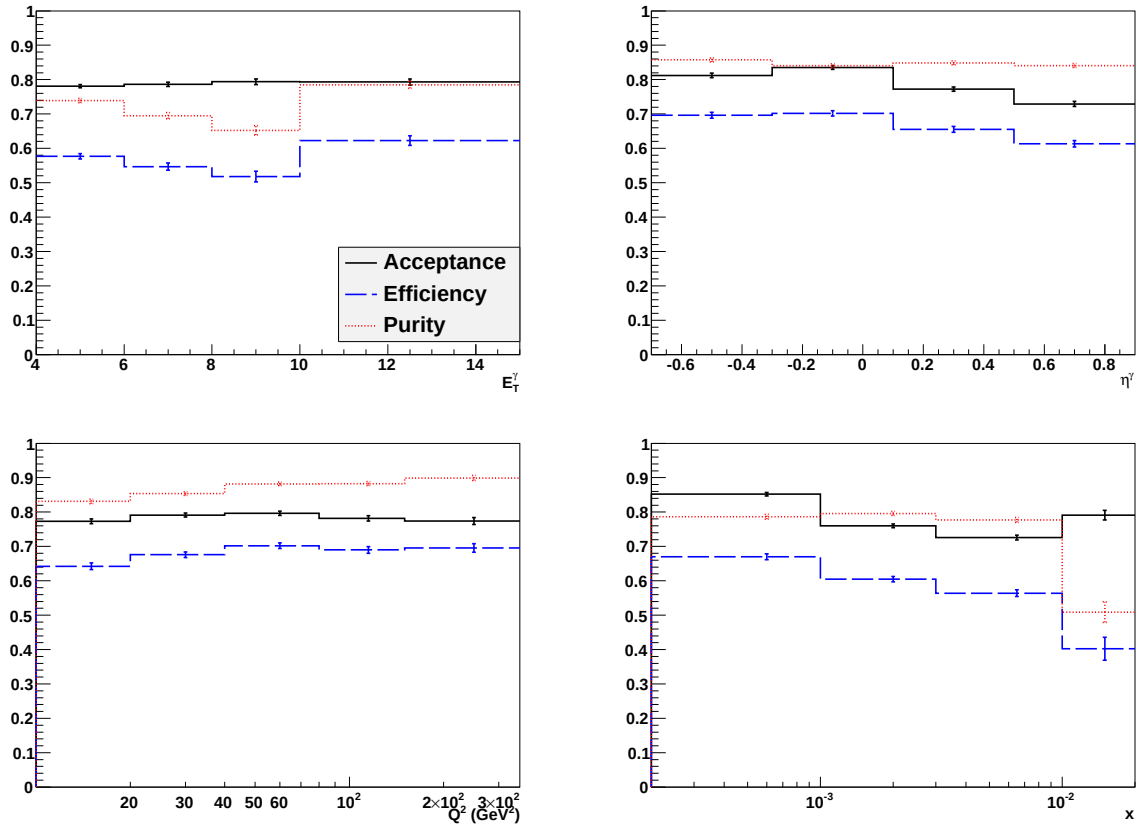

Figure 9.2: Acceptance (solid line), efficiency (dashed line) and purity (dotted line) as function of photon E_T^γ(top left) and η^γ(top right) and event Q^2(bottom left) and x(bottom right)

Fig. 9.2 shows the efficiency, purity and the acceptance as a function of E_T^γ, η^γ, Q^2 and x.

9.3 Cross-section calculations

The differential cross section is base on fitting the $\langle \delta z \rangle$ distribution as it has two important regions that are absent in f_{max} distribution. They are the photon peak close to 0 and the π^0 decay photons peak at 0.5. In PYTHIA Monte Carlo there

is the only high photon peak, and in ARIADNE background Monte Carlo sample there is not so high photon peak and very high peak of π^0 decay. The differential cross sections are calculated as the function of two photon characteristics, E_T^γ and η^γ, and also as the functions of two event variables, Q^2 and the Bjorken scale variable x. The differential cross sections of prompt photons (QQ) are presented together with predicted values of lepton high-energy radiation (LL). The predicted value of the prompt photons by Monte Carlo (PYTHIA) is scaled by the factor of 1.6 as it is underestimated and this factor was invented to compensate this underestimating to the total cross section.

The measured values of cross sections are the sum of the measured prompt photon cross section and the predicted lepton radiation cross section. The cross sections are shown in Figs 9.3 and 9.4.

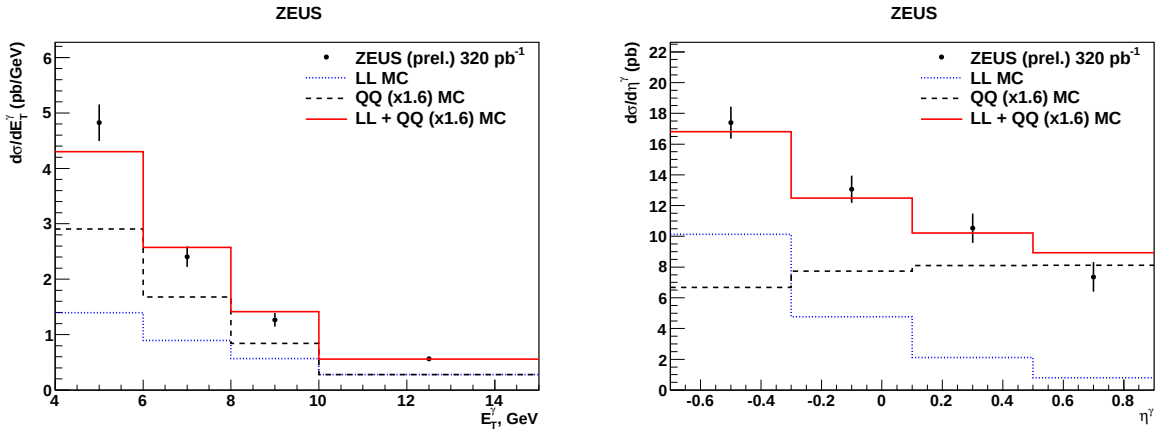

Figure 9.3: Inclusive differential E_T^γ(left) and η^γ(right) cross-sections

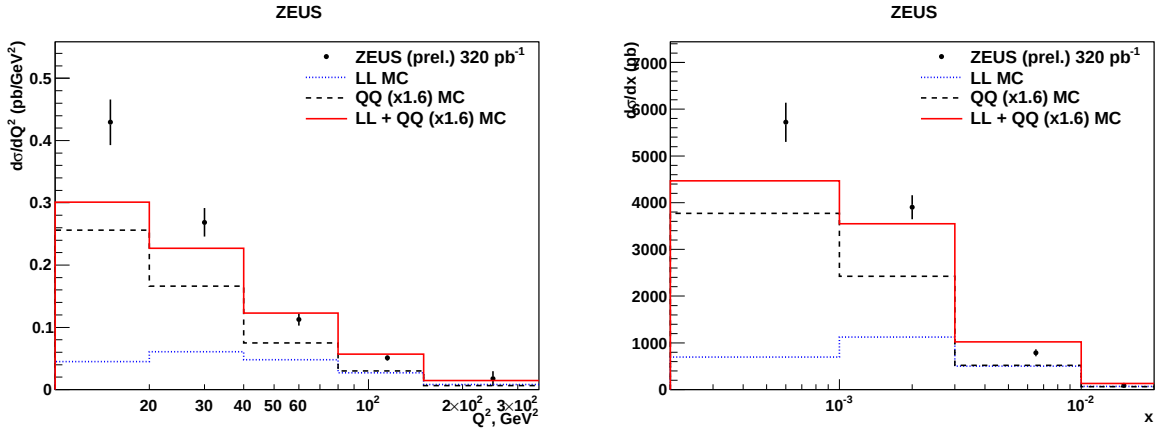

Figure 9.4: Inclusive differential Q^2(left) and x(right) cross-sections

Evaluated inclusive cross-sections are listed in tables 9.1 - 9.4.

E_T^γ(GeV)	$d\sigma/dE_T^\gamma$ (pb/GeV)
$4 < E_T^\gamma < 6$	3.4 ± 0.3
$6 < E_T^\gamma < 8$	1.51 ± 0.18
$8 < E_T^\gamma < 10$	0.70 ± 0.12
$10 < E_T^\gamma < 15$	0.28 ± 0.04

Table 9.1: Inclusive differential cross-section as a function of E_T^γ

η^γ	$d\sigma/d\eta^\gamma$ (pb)
$-0.7 < \eta^\gamma < -0.3$	7.3 ± 1.0
$-0.3 < \eta^\gamma < 0.1$	8.3 ± 0.9
$0.1 < \eta^\gamma < 0.5$	8.4 ± 0.9
$0.5 < \eta^\gamma < 0.9$	6.6 ± 1.0

Table 9.2: Inclusive differential cross-section as a function of η^γ

For making a cross-check of the results, the total cross section using integration of four differential cross sections can be calculated:

$\sigma_{E_T^\gamma} = \int \frac{d\sigma}{dE_T^\gamma} dE_T^\gamma = 12.7 \pm 1.5$ pb.

$\sigma_{\eta^\gamma} = \int \frac{d\sigma}{d\eta^\gamma} d\eta^\gamma = 12.2 \pm 3.0$ pb.

$\sigma_{Q^2} = \int \frac{d\sigma}{dQ^2} dQ^2 = 12.3 \pm 4.5$ pb.

$\sigma_x = \int \frac{d\sigma}{dx} dx = 11.6 \pm 5.8$ pb.

During the summation the last bins of Q^2 ($150 < Q^2 < 350$ GeV^2) and x ($0.01 < x < 0.02$) cross sections were not taken into account since it has limited statistics and the fit in these bins is not reasonable. As we see, the results are compatible within the statistical errors.

Q^2 (GeV^2)	$d\sigma/dQ^2$ (pb/GeV^2)
$10 < Q^2 < 20$	0.38 ± 0.04
$20 < Q^2 < 40$	0.21 ± 0.02
$40 < Q^2 < 80$	0.0643 ± 0.0095
$80 < Q^2 < 150$	0.024 ± 0.004

Table 9.3: Inclusive differential cross-section as a function of Q^2

x	$d\sigma/dx$ (pb)
$0.0002 < x < 0.001$	5030 ± 420
$0.001 < x < 0.003$	2780 ± 250
$0.003 < x < 0.01$	290 ± 70

Table 9.4: Inclusive differential cross-section as a function of x

10 Prompt Photon + Jet Production

10.1 Event selection

Prompt photons + jet analysis needs additional event selection for the jets. The prompt photon selection remains the same as defined in chapter 6.3. Jets are found as energy flow objects, ZUFOs, combining information from the calorimeter cells and tracks using the KTCLUS algorithm implemented to ORANGE software. For jet energy corrections, KTJET [18] offline implementation was used. Additional jet requirements are as follows:

- $E_{T,jet}^{corrected} > 6$ GeV. Here used the corrected transverse energy. Only high-energy jets are considered as they are produced in hard scattering processes.
- $-1.5 < \eta^{jet} < 1.8$. This selection suppress the jets that was found from proton remnant and that are not the objects of interest.

There were found 840 events with prompt photon plus jet. The jet requirement reduce the number of events by the factor of 3.6.

10.2 Jet variables

As shown in chapter 9, the photon characteristics differ. That is why it is obvious that jet parameters also should be different. The transverse energy and the pseudorapidity of the jet after event selection is shown on Fig.10.1.

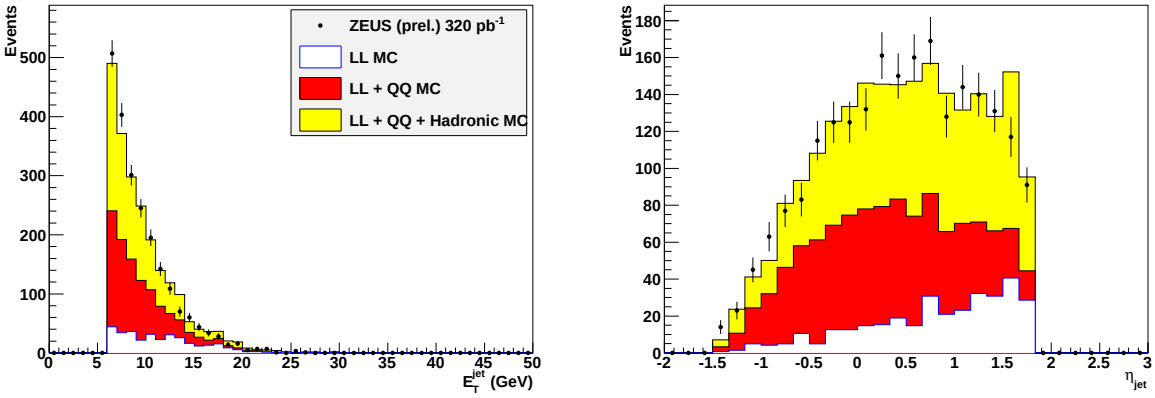

Figure 10.1: Transverse energy (left) and pseudorapidity (right) of the jet

10.3 Efficiency, purity, acceptance correction

Efficiency, purity and acceptance are calculated in the same way as for the inclusive values, adding the jet selection. The procedure is the same. The values of efficiency, purity and acceptance are presented on the Fig. 10.2. As seen, these values are a bit less comparing with the inclusive analysis values. This means that registering jets add some difficulties for the detector and thus it register less jets than were generated and found by the jet algorithm on hadron level.

10.4 Cross sections

Cross sections are calculated in the same way described in chapter 9.3 with additional jet requirements. The results are shown in Fig.10.3 and 10.4. The cross sections are presented as the same functions as for inclusive prompt photon analysis.

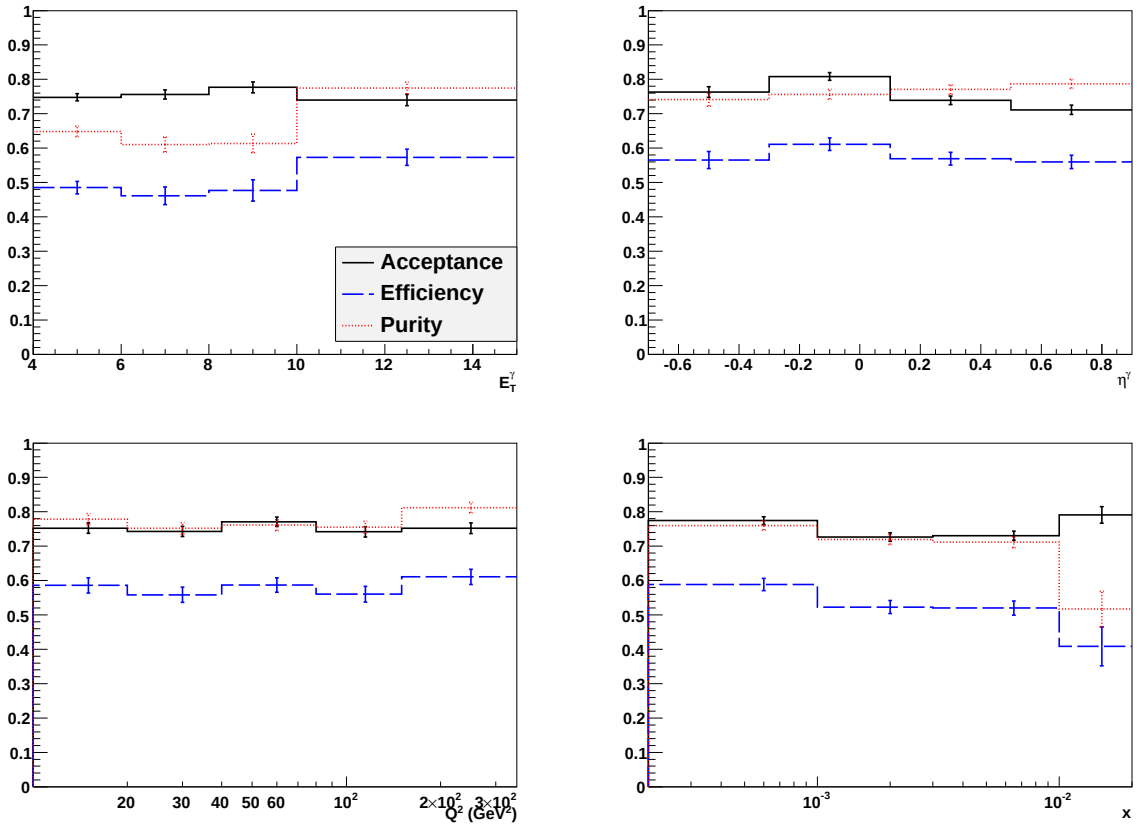

Figure 10.2: Acceptance (solid line), efficiency (dashed line) and purity (dotted line) as function of photon E_T^γ(top left) and η^γ(top right) and event Q^2(bottom left) and x(bottom right)

The values of calculated cross section are presented in the tables 10.5 - 10.8.

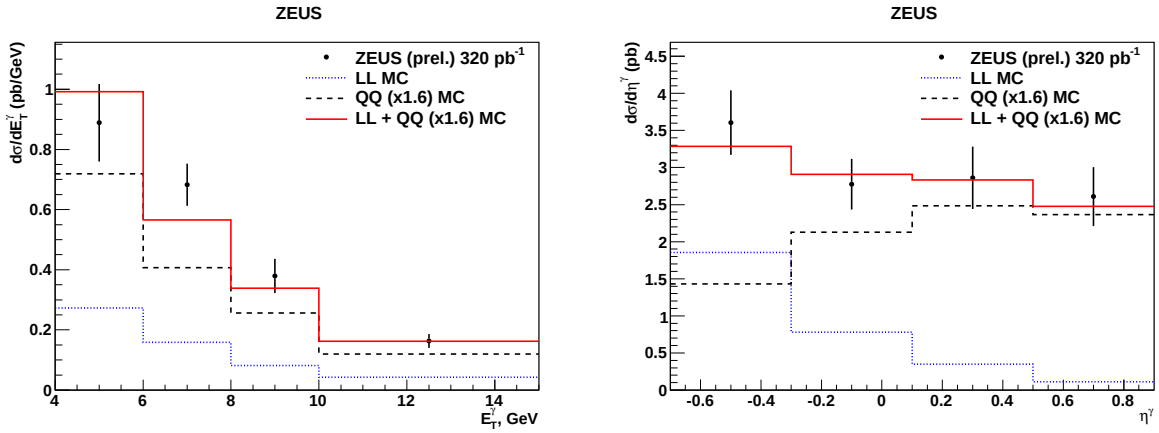

Figure 10.3: Photon plus jet differential E_T^γ(left) and η^γ(right) cross-sections

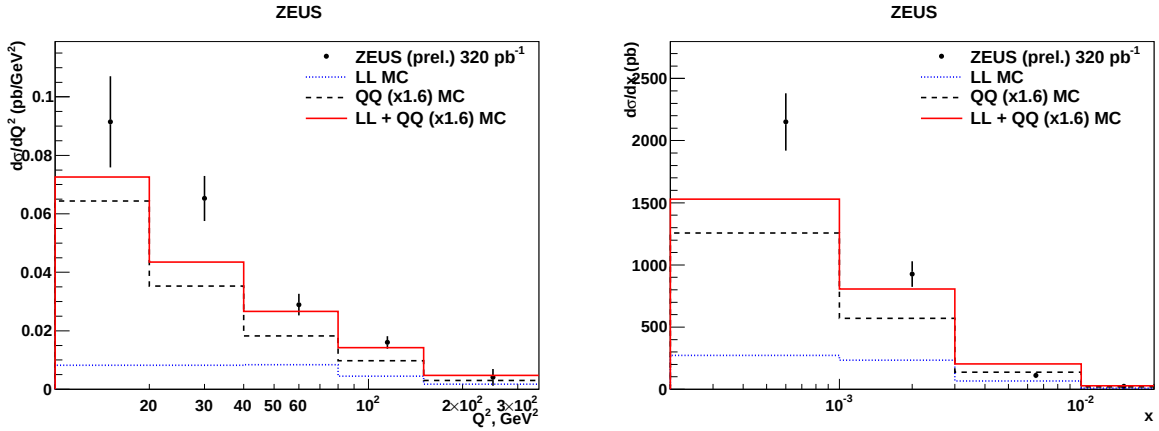

Figure 10.4: Photon plus jet differential Q^2(left) and x(right) cross-sections

Integrated cross section:

$$\sigma_{E_T^\gamma} = \int \frac{d\sigma}{dE_T^\gamma} dE_T^\gamma = 3.5 \pm 0.6 \text{ pb}.$$

$$\sigma_{\eta^\gamma} = \int \frac{d\sigma}{d\eta^\gamma} d\eta^\gamma = 3.5 \pm 1.2 \text{ pb}.$$

$$\sigma_{Q^2} = \int \frac{d\sigma}{dQ^2} dQ^2 = 3.6 \pm 1.8 \text{ pb}.$$

$$\sigma_x = \int \frac{d\sigma}{dx} dx = 3.2 \pm 2.4 \text{ pb}.$$

Again, the values are compatible within the statistical errors. Analyzing these results, we can say that the E_T^γ cross section is measured with the best precision,

E_T^γ(GeV)	$d\sigma/dE_T^\gamma$ (pb/GeV)
$4 < E_T^\gamma < 6$	0.62 ± 0.12
$6 < E_T^\gamma < 8$	0.52 ± 0.07
$8 < E_T^\gamma < 10$	0.30 ± 0.06
$10 < E_T^\gamma < 15$	0.120 ± 0.022

Table 10.5: Photon plus jet differential cross-section as a function of E_T^γ

η^γ	$d\sigma/d\eta^\gamma$ (pb)
$-0.7 < \eta^\gamma < -0.3$	1.8 ± 0.4
$-0.3 < \eta^\gamma < 0.1$	2.0 ± 0.3
$0.1 < \eta^\gamma < 0.5$	2.5 ± 0.4
$0.5 < \eta^\gamma < 0.9$	2.5 ± 0.4

Table 10.6: Photon plus jet differential cross-section as a function of η^γ

and thus it shows that probably this parameter is better measured by the detector than anothers.

11 Conclusions

The production of inclusive prompt photons and prompt photon plus jet in deep inelastic lepton-proton scattering has been observed and measured using the ZEUS detector. The data were taken from $e^{\pm}p$ collision during the 2004-2007 HERA running period and correspond to the integrated luminosity of $320pb^{-1}$. The cross-section was measured and presented as a function of photon variables, transverse energy, in the kinematic region $4GeV < E_T^\gamma < 15GeV$ and pseudorapidity, in the region $-0.7 < \eta^\gamma < 0.9$, and also as the function of the event variables, photon virtuality Q^2 in the region of $10 < Q^2 < 150\text{GeV}^2$ and Bjorken scale variable, x in the region $0.0002 < x < 0.02$. The x cross section is the first measurement at HERA.

The signal extraction was made in 3 stages: 1) event selection of DIS events; 2) extraction of prompt photon (plus jet) signal; 3) fitting Monte Carlo signal for extracting the number of events with prompt photons. The number of found

$Q^2(\mathrm{GeV}^2)$	$d\sigma/dQ^2$ (pb/GeV^2)
$10 < Q^2 < 20$	0.083 ± 0.016
$20 < Q^2 < 40$	0.057 ± 0.008
$40 < Q^2 < 80$	0.021 ± 0.004
$80 < Q^2 < 150$	0.0115 ± 0.0021

Table 10.7: Photon plus jet differential cross-section as a function of Q^2

x	$d\sigma/dx$ (pb)
$0.0002 < x < 0.001$	1880 ± 230
$0.001 < x < 0.003$	690 ± 100
$0.003 < x < 0.01$	44 ± 21

Table 10.8: Photon plus jet differential cross-section as a function of x

prompt photon events is about $N_\gamma = 3100$ in the selected phase space, and of them $N_{\gamma+jet} = 840$ events with the accompanying jet. The total cross section was measured to be $\sigma^{total}_{ep\to\gamma X} = 12.7 \pm 1.5$ for DIS prompt photon events and $\sigma^{total}_{ep\to\gamma jet\ X} = 3.5 \pm 0.6$. In order to compare the recent results with the previous one, Q^2 was changed back to $Q^2 > 35\mathrm{GeV}^2$. These results are compatible with previous ones [15].

References

[1] *HERA - A Proposal For A Large Electron Proton Colliding Beam Facility At DESY, (unpublished)*, internal note DESY-HERA-81-10, 1981

[2] A. Gehrmann-De Ridder, T. Gehrmann, E. Poulsen, Phys.Rev.Lett. **96**:132002 (2006)

[3] A.D. Martin, R.G. Roberts, W.J. Stirling, R.S. Thorne, Eur. Phys. J. C**39**:155-161 (2005)

[4] $http://www-zeus.desy.de$

[5] $http://www-h1.desy.de$

[6] G. van der Steenhoven *Review of HERMES experiment*, Prog. Part. Nucl. Phys. 55(2005) 181-197

[7] U.Ulwer, *Status and commissioning results from HERA-B*, Nucl. Meth. Phys A 462 (2001) 202-211

[8] ZEUS Collaboration, U Holm(ed.), *The ZEUS Detector. Status report (unpublished)*, DESY, 1993, available at $http://www-zeus.desy.de/bluebook/bluebook.html$

[9] ZEUS Collaboration (B.Foster et al.), *The design and construction of the ZEUS Central Tracking Detector*, Nucl. Inst. Meth. A338, 254, 1994

[10] R.Clanner *Test program for the ZEUS Calorimeter*, Nucl. Meth. Phys. A 265 (1988) 211-209

[11] S.Chekanov, S. Magill, *Initial Perfomance of the ZEUS Barrel Presampler*, ZEUS 00-006 (2000)

[12] Sung Won Lee, *Measurements of Prompt Photon Photoproduction at HERA*, Ph. D. Thesis, Glasgow university, Glasgow (2000)

[13] $http://www-zeus.desy.de/ZEUS\_ONLY/analysis/orange/index.html$

[14] $http://root.cern.ch$

[15] ZEUS Collaboration, S.Chekanov et al., Phys. Lett. B **595** (2004) p.86-100

[16] Mairi Siobhan Bell, *Prompt Photon Production in Deep Inelastic Scattering at HERA*, Ph. D. Thesis, Glasgow (2003)

[17] J.Huth et al., Proc. *Summer Study on High Energy Physics*, Snowmass (1990)

[18] J. M. Butterworth, J. P. Couchman, B. E. Cox, B. M. Waugh, **arXiv:hep-ph/0210022v1**

[19] M. Cacciari and G. P. Salam, Phys. Lett. B **641** (2006) p.57 **arXiv:hep-ph/0512210**

[20] T.Sjoestrand *PYTHIA 6.4 Physics and manual*, Fermilab-pub, 2006, 478

[21] *http* : *//wwwasdoc.web.cern.ch/wwwasdoc/minuit/minmain.html*

[22] J.Taylor *An Introduction to Error Analysis*, (in Russian) , Moscow, "Mir", 1985, 272 pages.